Computers in Biology and Medicine 194 (2025) 110473

Contents lists available at ScienceDirect

Computers in Biology and Medicine

journal homepage: www.elsevier.com/locate/compbiomed

Transport and deposition of inhaled fibers in a realistic female airway model: A combined experimental and numerical study

František Prinz [a,*], Jana Kánská [a], Jakub Elcner [a], Ondřej Hájek [a], Adrian Kummerländer [b], Mathias J. Krause [b], Miroslav Jícha [a], František Lízal [a]

[a] Brno University of Technology, Technicka 2896, Brno, 616 69, Czech Republic
[b] Karlsruhe Institute of Technology, Kaiserstraße 12, Karlsruhe, 76131, Germany

ARTICLE INFO

Keywords:
Fiber transport
Deposition
In vitro
In silico
Female airway geometry
Lattice Boltzmann method
Euler–Lagrange Euler-rotation

ABSTRACT

This study presents a combined experimental and numerical investigation of fiber transport and deposition in a realistic model of the female respiratory tract, extending to the seventh generation of branching. Numerical simulations were performed using the Euler–Lagrange Euler-Rotation (ELER) method, an efficient alternative to conventional Finite Volume Methods that benefits from explicit formulation and vast scalability, enabling fast parallelization on high-performance clusters. The ELER method was coupled with the Lattice Boltzmann Method (LBM) to simulate fiber dynamics under a realistic inspiratory flow profile. Experimental validation was conducted using an identical physical airway replica. The results demonstrated good agreement between simulations and experiments in the upper airways and trachea, with some discrepancies in the bifurcations, likely owing to the challenges of modeling complex turbulent flow with ELER. This method is more accurate than corresponding effective diameter simulations. Deposition patterns were analyzed as a function of fiber dimensions, revealing higher accuracy of the ELER method for smaller particles and confirming the tendency of higher aspect ratio fibers to penetrate deeper into the lungs. The orientation-dependent deposition mechanism was deployed, underscoring the importance of solving the actual orientations of the fibers. While advancing our understanding of fiber transport in female airways, the findings also reveal limitations in current numerical techniques, particularly in bifurcations. This study emphasizes the distinct behavior of fibrous versus spherical particles, with fibers exhibiting a greater propensity to reach deeper lung regions, which has significant implications for inhalation toxicology and drug delivery.

1. Introduction

The study of particle transport and deposition within the human respiratory system is essential for understanding various physiological and pathological processes as well as for developing effective drug delivery strategies. While considerable research has focused on male airway models, there is a growing recognition of the need to investigate female-specific airway geometries due to significant anatomical and physiological differences between sexes [1–3]. Females exhibit smaller airway diameters, particularly in the pharynx and velopharynx [4], differences in lung volume and breathing patterns [5], and hormonal influences that can affect airway responsiveness [6]. These differences can influence airflow patterns, particle deposition, and ultimately, the efficacy and safety of inhaled therapies [7]. To address this gap in our understanding of female-specific aerosol deposition, our study utilizes a realistic female airway model supplemented with tidal volume and a breathing pattern typical for females.

Fibrous particle transport has significant implications in both safety and engineering applications. Various man-made fibers are crucial components of composite materials and filtration systems used across many industries, such as carbon fibers in aerospace composites and glass fibers in air filtration systems. Although exposure to toxic fibers such as asbestos is a severe health hazard, biodegradable fibers offer unique possibilities for targeted drug delivery [8].

Numerical simulation of the transport of non-spherical particles is more complex than of spherical particles due to the nonsymmetric shape, and hence experimental studies *in vitro* are indispensable. However, only a few experimental studies focusing on the deposition of fibers in human airways have been conducted. Marijnissen et al. [9] and Myojo and Takaya [10] used simplified models of a bifurcation for deposition experiments. The latter experimentally examined the deposition of fibers in Weibel's [11] idealized geometry up to the fourth generation of airway branching, even with cyclic breathing. Su and

* Corresponding author.
E-mail address: frantisek.prinz@vutbr.cz (F. Prinz).

https://doi.org/10.1016/j.compbiomed.2025.110473
Received 27 January 2025; Received in revised form 14 May 2025; Accepted 26 May 2025
Available online 12 June 2025

Cheng [12] conducted experimental investigations on the deposition of carbon fibers with lengths ranging from 10 to 150 μm, using a realistic airway model extending beyond the fourth generation. At a flow rate of 15 $\mathrm{l\,min^{-1}}$, the majority of fibers were deposited in the upper respiratory tract, comprising the oral cavity, pharynx, and larynx, whereas 63% passed through the replica without deposition. At higher flow rates, 43.5 $\mathrm{l\,min^{-1}}$ and 60 $\mathrm{l\,min^{-1}}$, the deposition rate increased, with the fibers primarily deposited in the oropharynx and larynx. The deposition efficiency in the oral cavity was significantly lower than that in the nasal cavity. These findings agree with the results of a later simulation study by Feng et al. [13].

Subsequently, Su and Cheng [14] demonstrated that inertial impaction was the dominant deposition mechanism in the oral cavity. Furthermore, Zhou et al. [15] performed experiments using two lung models: one with the oral cavity half open and the other fully open, where the degree of opening influenced the angle of attachment to the oropharynx. Su and Cheng [16] conducted experiments using three types of materials, namely glass, TiO_2, and carbon fibers, at three distinct inhalation flow rates. In contrast to their previous studies focused on carbon particles, the fibers exhibited minimal deposition within the model, irrespective of their length or inhalation flow rate. The authors attributed these results to the relatively low momentum of the lightweight fibers, which enabled them to more effectively follow airflow dynamics in the airways. They indicated that these fibers do not demonstrate a significant deposition within the airways up to the third generation of branching, thereby facilitating their penetration deeper into the lungs. In contrast, fibers with greater momentum were observed to deposit in the oral cavity, allowing for potential removal through swallowing.

Bělka et al. [17] experimentally investigated the deposition of glass fibers in a respiratory tract replica extending from the oral cavity to the 7th bifurcation. The fiber deposition within the model was minimal, with deposition fractions of 0.7% at a steady flow rate of 15 $\mathrm{l\,min^{-1}}$, 1.9% at 30 $\mathrm{l\,min^{-1}}$, and 4.6% at 60 $\mathrm{l\,min^{-1}}$. Higher deposition occurred in the oral cavity and more complex segments.

Lizal et al. [18] conducted one of the rare experimental studies focusing on the visualization of fiber movement in the simplified model of the respiratory tract. They produced a high-speed camera recording of fibers at specific recording frames in a straight tube and upstream and downstream of the bifurcation for several flow rates. A robust statistical evaluation showed two dominant orientations, parallel and perpendicular to the streamlines, and a significantly higher probability of flips downstream of the bifurcation than those in the straight tube.

In addition to experimental studies, several researchers have studied fiber transport and deposition employing computational fluid and particle dynamics (CFPD) simulations *in silico*. The available simulation approaches were summarized by Feng and Kleinstreuer [19]. A popular choice is the one-way coupling simplified Euler–Lagrangian approach. Here, the fibers are treated as dilute, and rotational movement is neglected. The primary influence on the trajectory comes from the computation of the shape factor C_D where either empirical correlations (e.g., Lasso and Weidman [20], Haider and Levenspiel (H–L) [21], Tran-Cong (T-C) [22]), or theoretical formulations (Stober [23]) are used. Inthavong [24] compared the H–L and T-C models in simulating the nasal cavity at a rather low flow rate of 7.5 $\mathrm{l\,min^{-1}}$ and showed good agreement for particles smaller than 100 μm. This study was extended by Farkas et al. [25] to a realistic male model using the same airway replica as that used by Belka et al. [17] for three stationary flow rates. Chen et al. [26] investigated a single idealized bifurcation under steady laminar flow conditions. They showed that gravity affects the deposition characteristics. Orientations of deposited fibers were obtained from micrographs. The prevalent orientation was parallel with deviations mainly in the bifurcations emphasizing the effect of interception. Supporting numerical simulations used equivalent sphere approaches.

With the increase in computational power in recent decades, methods that account for rotational motion have been used accordingly. Tian et al. [27] presented the Euler–Lagrange Euler-Rotation (ELER) approach and validated it by means of the deposition fraction in a straight tube for low Reynolds numbers. In a follow-up study, this team [28] numerically investigated carbon fibers in the range of aspect ratio $1 < \beta < 80$ on a more extensive idealized model, from the trachea to the third bifurcation, and showed different rotational behaviors when passing the bifurcations. Shanley et al. [29] deployed ELER in a realistic nasal airway model under steady laminar conditions and proposed two empirical models for pressure drop and deposition efficiency.

Shachar-Berman et al. [8] investigated the total breathing maneuver mimicking the Dry Powder Inhaler (DPI) profile with a peak flow rate of 90 $\mathrm{l\,min^{-1}}$ for an average adult in a semi-realistic model up to the 9th generation of branching, and ideal fiber dimensions for medical treatment were suggested. Li et al. made significant contributions to the ELER modeling of non-spherical particles in the respiratory tract. In their initial study [30], they simulated fiber transport in a realistic nasal cavity, demonstrating complex translational and rotational behavior. While the fibers were generally aligned with streamlines, occasional quick flips were observed. Subtle deviations in trajectory and rotation can significantly impact deposition patterns, highlighting the importance of accurate interception modeling. In a follow-up study, Li et al. [31] investigated the effects of shear-induced lift forces on non-spherical particles in a circular duct. This force caused a lateral drift, potentially dominating the deposition forces and emphasizing the importance of its consideration. In their most recent study, Li et al. [32] numerically investigated fiber transport and deposition in an extended human airway model up to the 15th generation, which is a rare scope for such studies. The evaluation of the deposition for three different aspect ratios confirmed the significance of both the aspect ratio and aerodynamic diameter in influencing the deposition curves.

Kiasadegh et al. [33] compared steady and cyclic regimes in a realistic model of a 24-year-old female airways down to the trachea. They emphasized the importance of transient simulation, showing significant differences in deposition fractions and penetration depth compared with steady-state simulations, especially for fibers heading deeper into the lungs. In that study, a sinusoidal inspiration profile was prescribed. Tavakol et al. [34] investigated fiber deposition in nasal cavities using the ELER method coupled with Reynolds Averaged Navier–Stokes (RANS) simulations, incorporating random walk models to account for turbulent fluctuations under steady flow conditions. In a consecutive study, Abolhassantash et al. [35] deployed force formulations for non-creeping flow conditions, derived by Zastawny et al. [36] and Ouchene et al. [37], and compared them with conventional creeping flow formulations within the ELER framework for simulations in a female nasal passage under steady conditions. Greater differences between the non-creeping and creeping formulations were observed for flow rates above 20 $\mathrm{l\,min^{-1}}$ and with increasing fiber aspect ratio. Furthermore, a comprehensive comparison of different random walk models used in conjunction with RANS simulations was conducted by Mofakham et al. [38]. Finally, recent progress in the computational modeling of fiber transport was summarized by Tian and Ahmadi [39].

Most of the aforementioned studies have been either experimental or numerical. In contrast, our combined experimental and computational research not only allows for a comparison of the total deposition in each segment of the airways but also enables a broader analysis depending on the fiber dimensions. The utilization of female realistic geometry with a realistic inspiration cycle enables focusing on the differences compared to male geometry, which has been commonly studied in the past. Building upon the previous studies of Henn et al. [40] and Prinz et al. [41], this study extends the application of the Lattice Boltzmann Method (LBM) beyond spherical particles. Specifically, the ELER approach is employed as the particle tracking algorithm and coupled with the LBM to simulate the transport and

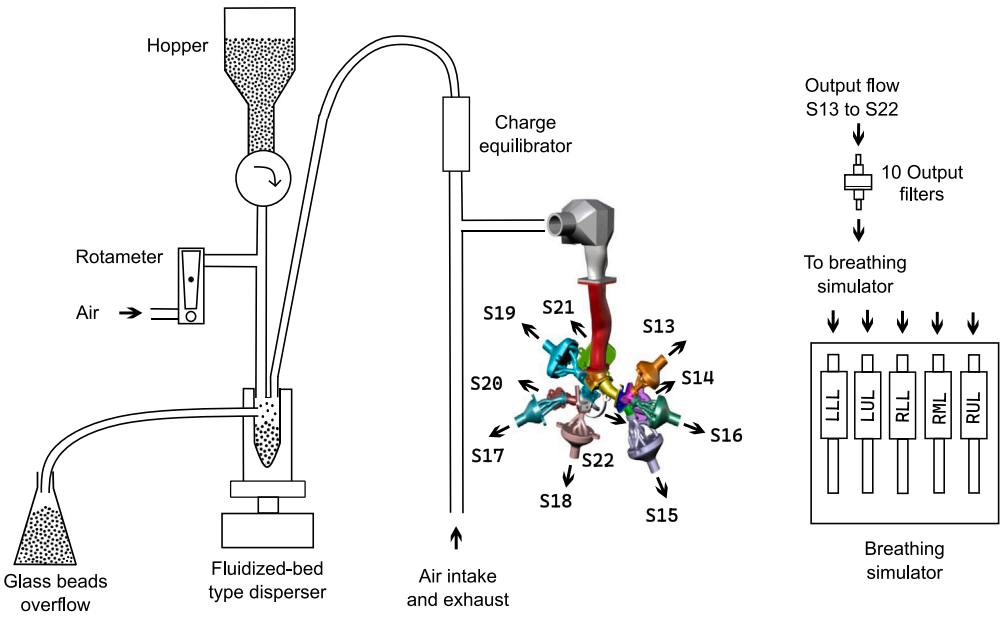

Fig. 1. Schematic of the experimental setup used to investigate fiber deposition in a realistic female airway model.

deposition of fibrous particles. This novel combination allows for a more accurate representation of fiber dynamics compared with simplified models, particularly in complex flow regimes found in bifurcations. Specifically, we aim to answer the following research questions:

What is the distribution of deposited inhaled fibers within various segments of the female respiratory tract? What is the influence of fiber dimensions (length and diameter) on the deposition patterns? How do the experimental results compare to the numerical simulations using the LBM-ELER approach, and what are the potential sources of discrepancies? How does particle release time during the inspiration cycle affect the deposition fraction and location?

The remainder of this paper is organized as follows. Section 2 describes the experimental setup and numerical methods employed, including the LBM-ELER approach and geometry used. Section 3 presents the results of both the experimental and numerical investigations, followed by a discussion comparing the two approaches and analyzing the influence of fiber dimensions and release time. Section 4 discusses the limitations of the current study. Section 5 summarizes the key findings and concludes the study.

2. Methods

2.1. Experimental setup

This section describes the experimental setup used to investigate the deposition of glass fibers in a realistic female airway model. The scheme of the experimental setup is shown in Fig. 1 and described in detail below.

Polydisperse glass fibers with diameters ranging from 1 to 10 μm and lengths ranging from 5 to 100 μm were used in the experiments. The samples were obtained by crushing glass wool (Supafil Loft, Knauf Insulation GmbH) in a crusher. The fibers were mixed with glass beads (Ballotini Impact Beads, Potter Industries Inc.) and sieved to improve the ensuing deagglomeration and dispersion of fibers within the airway replica. The mixture consisted of 2% fibers and 98% beads.

The prepared mixture of glass fibers and beads was introduced into the experimental setup using a hopper, as shown in Fig. 1. From the hopper, the mixture flowed into a rotary feeder, which delivered it to a fluidized-bed disperser. Within the disperser, the fibers and beads were separated, and the aerosolized fibers were then transported to a charge equilibrator (NEKR-10, Eckert and Ziegler CESIO) to neutralize their electrostatic charges. The neutralized fibers were subsequently conveyed to the airway replica through a tube connected to the air intake and exhaust system of the laboratory. This connection ensured a controlled environment and prevented the leakage of fibers into the laboratory.

A realistic replica of the female airway, used here for the first time, was employed in this study. It was derived by applying a uniform linear scaling factor of 0.88 to a previously validated male airway model [17,42]. This factor was determined through a comparative analysis of key anatomical dimensions reported in the literature for representative adult male and female respiratory tracts [43–45]. Specifically, metrics such as tracheal length and mean luminal cross-sectional area served as primary parameters considered in deriving this average scaling factor to represent overall size differences between the sexes. The replica spans from the oral cavity to the seventh generation of the lung bifurcation, and the remainder of the lung is replaced by output filters. The model was capable of simulating breathing patterns using an original breathing simulator, which reproduced the specific patterns of the five lung lobes: the right upper lobe (RUL), right middle lobe (RML), right lower lobe (RLL), left upper lobe (LUL), and left lower lobe (LLL). A model of the geometry with its segmentation is depicted in Fig. 2. To enhance particle adhesion and better simulate the trapping effect of the mucus layer found in vivo, the inner surfaces of the airway replica were coated with a thin layer of silicone oil prior to each experimental run. This surface treatment is a common practice in similar in vitro deposition studies [16,17].

To the best of our knowledge, experimental data on fiber deposition during realistic female inspiration are not available in the literature; therefore, we conducted experiments to fill this gap. The realistic breathing profiles used in this study (see Fig. 3) were derived from the data presented in the Annals of the ICRP [46]. Specifically, we scaled down the values reported in [46] by a factor of 0.8, based on a comparison of the tidal volumes for the male and female geometries in [46] and the realistic male airway model from which the current female geometry was derived [17]. The distribution of flow rates among the lung lobes was adapted from Jahani et al. [47], who analyzed four-dimensional computed tomography data of six breathing cycles averaged over one minute from healthy volunteers (50% women).

The airway replica was then exposed to aerosolized fibers. After exposure, two types of samples were collected: (a) samples from the output filters, which captured the fibers that passed through the entire

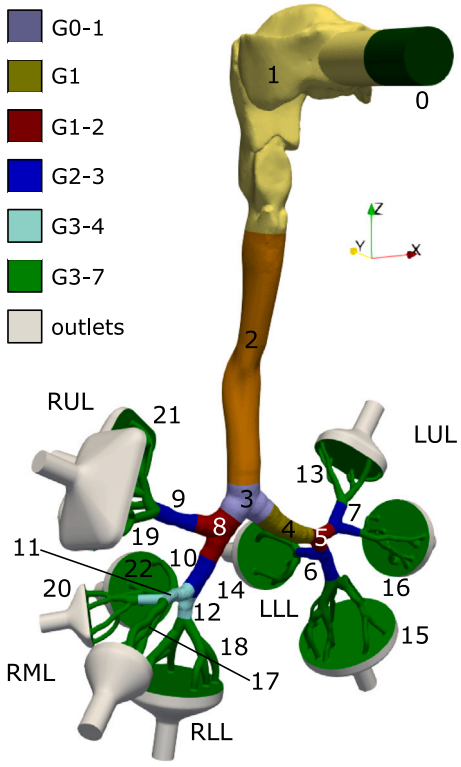

Fig. 2. Segmentation of the realistic female airway geometry with corresponding segment numbers. Each color represents a different airway generation, as indicated in the legend.

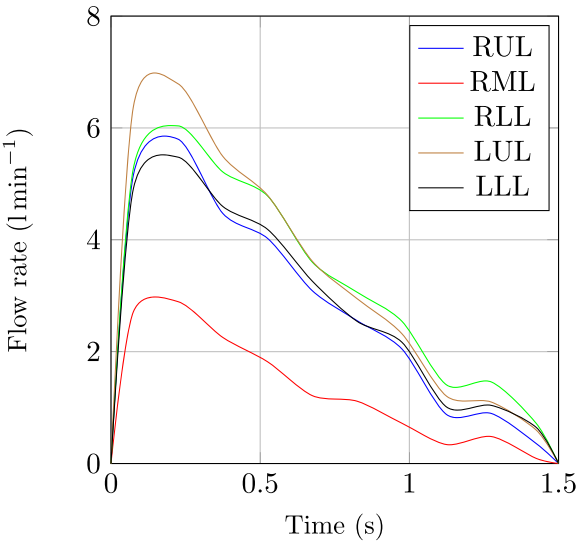

Fig. 3. Flow rate profiles for each lung lobe during the inspiration cycle [46,47].

replica, and (b) samples obtained from each individual segment of the replica. To collect the fibers deposited within the replica, it was first disassembled. Each segment was then placed in a beaker and immersed in isopropanol. The beaker was placed in an ultrasonic bath to dislodge any fibers adhering to the segment walls. This process created a suspension of fibers in isopropanol.

To analyze the fibers, the suspension was filtered through nitrocellulose membrane filters using a vacuum filtration pump. The filters were then dried and made transparent by placing them on a glass slide using an acetone vaporizer (QuickFix, EMS, USA). Samples from the output filters were made transparent in the same manner. Each sample was then manually evaluated under a phase-contrast microscope (Nikon Eclipse E200, Nikon, Tokyo, Japan) using a 40x objective and Walton-Beckett graticule (cf. representative sample Fig. A.22 in Appendix). Fiber counting was performed according to a method based on the WHO guidelines [48]. To ensure a representative count, 20 randomly selected areas were analyzed for each sample. Because of the polydispersity of the fibers, the diameter and length of each fiber were measured and recorded for further analysis.

2.2. Numerical simulation setup

This section outlines the numerical methods used to simulate the transport and deposition of fibers within the female airway model. Particle transport and deposition were numerically simulated using Computational Fluid and Particle Dynamics (CFPD). The solution was divided into two parts – the fluid flow solution and particle motion solution – coupled with the velocity field data, as described below. The simulation is considered as one-way coupling, and the discrete phase represented by the particles is dilute with a very low volume fraction (approximately 10^{-8}) and hence does not affect the flow field.

2.2.1. Fluid phase

Fluid flow modeling is based on the *Lattice Boltzmann Method* (LBM), a mesoscopic numerical approach to transport problems based on a discretization of the Boltzmann equation [49]. Due to its algorithmic structure, the LBM is uniquely suited for highly parallel execution on state-of-the-art high-performance computers [50]. Specifically, it is an efficient alternative [51] to conventional finite-volume methods, providing 32-fold performance improvements compared to OpenFOAM when fixing the numerical error in a fair comparison of an industrial reference case.

In LBM, the spatial simulation domain is discretized by a regular lattice on which populations $f(\vec{x},\vec{\xi},t)$, describing the state of the system,[1] propagate along discrete velocities $\vec{c}_i$ following a so called collision step that relaxes the per-cell populations towards their macroscopic equilibrium distribution:

$$f_i(\vec{x}+\vec{c}_i\Delta t, t+\Delta t) = \left(1-\frac{\Delta t}{\tau}\right) f_i(\vec{x},t) + \frac{\Delta t}{\tau} f_i^{(eq)}(\vec{x},t), \qquad \forall i \in \langle 0,18\rangle. \quad (1)$$

Here, $\vec{c}_i$ denotes the discrete velocity stemming from the velocity set D3Q19, $f_i^{(eq)}$ is the equilibrium distribution function and τ the relaxation time in the Bhatnagar–Gross–Krook (BGK) collision operator resolving the particle interactions. This equation can be divided into two steps, collision and streaming.

$$f_i^{\mathrm{coll}}(\vec{x},t) := \left(1-\frac{\Delta t}{\tau}\right) f_i(\vec{x},t) + \frac{\Delta t}{\tau} f_i^{(eq)}(\vec{x},t), \quad (2)$$

$$f_i^{\mathrm{str}}(\vec{x}+\vec{c}_i\Delta t, t+\Delta t) := f_i^{\mathrm{coll}}(\vec{x},t). \quad (3)$$

Macroscopic quantities are computed using discrete velocity moments

$$\rho(\vec{x},t) = \sum_i f_i, \quad \vec{u}(\vec{x},t) = \frac{1}{\rho}\sum_i f_i\vec{\xi}_i, \quad p(\vec{x},t) = \frac{\rho}{c_s^2}, \quad (4)$$

where ρ denotes the density of the fluid, $\vec{u}$ denotes the macroscopic velocity, p denotes the pressure, and c_s denotes the speed of sound. The Chapman-Enskog expansion [52] can be used to demonstrate the convergence of this method to solutions of the incompressible Navier–Stokes equations, justifying its use in the present application.

To model turbulent phenomena, a Large Eddy Simulation (LES) with the Smagorinsky subgrid-scale (SGS) model [53] was enabled (further implementation details are provided in [41]). The Smagorinsky constant was assigned the common value of 0.1. LES provides the time-varying large-scale turbulent velocity fields, which can capture

[1] $f(\vec{x},\vec{\xi},t)$ explicitly describes the probability of the total mass of particles in position $\vec{x}$ with microscopic velocity $\vec{\xi}$ in time t.

the majority (e.g., > 80%) of the turbulent kinetic energy in well-resolved simulations [54]. The influence of smaller subgrid eddies on particle dispersion is commonly accounted for in RANS simulations through models such as random walk approaches [55]. For LES, while SGS turbulent dispersion effects can be modeled, their impact on the deposition of micrometer-sized particles has been reported as relatively small in certain contexts (e.g., [56,57]. Consequently, explicit modeling of SGS particle turbulent dispersion has often not been included in LES studies of airflow and deposition in the respiratory tract [58]. Supporting this approach, Koullapis et al. [59] demonstrated in a benchmark comparison that LES models without explicit SGS turbulent dispersion for particles achieved reasonable accuracy against experimental data for regional deposition in human airways. Based on these considerations from the literature and the common practice in the field, explicit modeling of SGS turbulent dispersion effects on particle trajectories was not included in the present study, though it remains an important area for future research.

A pressure boundary condition, as proposed by Skordos [60], was imposed at the mouth inlet. At the outlets, uniform velocity boundary conditions, as proposed by Skordos [60], were prescribed, with time-dependent velocities calculated from a realistic inspiration profile (Fig. 3) and the corresponding tidal volume distributions. Velocities were implemented using a linear interpolation scheme. Two consecutive inhalations were simulated with a reduced hold-up time of 0.25 s between them. Each lung lobe in our model contains two funnels, which are connected to the respective lobe pistons of the breathing simulator. The flow rate distribution between the funnels in the simulation was set based on the experimental measurements. To reduce the computational cost, the simulation did not include the connection hoses and pistons. The interpolated bounce-back scheme at airway walls by Bouzidi [61] was employed to ensure second-order convergence and resolve the highly curved complex geometry features. The suitability of this boundary condition is supported by the flow regime; the Reynolds number (Re) in the main bifurcation reaches a maximum of approximately 3030 at the peak flow rate, indicating flow regime transiting to turbulent at its maximum rather than a highly turbulent state. While resolving the viscous sublayer accurately can be challenging with this method in highly turbulent flows, it provides acceptable accuracy for the conditions simulated here. This approach has also been successfully deployed in similar LBM airway simulations by Lintermann et al. [62].

2.2.2. Particle phase

The motion of the fibers was computed using the ELER method, as presented by Tian et al. [27]. This is an extension of the classical Lagrangian approach, which accounts for the orientation and rotational movement of the fibers by solving Euler's equations. Therefore, this method is more accurate than other methods that use an equivalent diameter, where the exact orientation is neglected.

For the numerical computation of forces and torques, fiber orientation is crucial. For clarity, three coordinate systems are used.

- the laboratory coordinate system (xyz),
- the particle co-moving coordinate system ($x'y'z'$) aligned with the laboratory coordinate system with its origin at the particle's center of mass, and
- the particle coordinate system ($x''y''z''$) where the z'' axis is aligned parallel to the axis of symmetry of the spheroid.

The fibers are approximated by prolate spheroids (i.e., prolate ellipsoids generated by rotating an ellipse around its major axis), as shown in Fig. 4(a).

The transformation between the co-moving and particle frame of reference is given by

$$\vec{x}' = \mathbf{A}\vec{x}'' \tag{5}$$

where $\mathbf{A}$ denotes a transformation matrix. $\mathbf{A}$ can be expressed in two ways, using Euler's angles or Euler's quaternions. For numerical purposes, Euler's quaternions (x-convention) are more suitable for yielding convergence in all situations in contrast to Euler's angles [63]. These are defined by four parameters $(\varepsilon_1, \varepsilon_2, \varepsilon_3, \eta)$ in relation to a unit vector that determines the rotational axis $\vec{i}$ and rotation angle Ω using the following definitions:

$$\begin{pmatrix} \varepsilon_1 \\ \varepsilon_2 \\ \varepsilon_3 \end{pmatrix} = \vec{i}\sin\left(\frac{\Omega}{2}\right), \qquad \eta = \cos\left(\frac{\Omega}{2}\right), \tag{6}$$

as shown in Fig. 4(b). The transformation matrix $\mathbf{A}$ is given by the relation

$$\mathbf{A} = \begin{pmatrix} 1-2(\varepsilon_2^2+\varepsilon_3^2) & 2(\varepsilon_1\varepsilon_2+\varepsilon_3\eta) & 2(\varepsilon_1\varepsilon_3-\varepsilon_2\eta) \\ 2(\varepsilon_2\varepsilon_1-\varepsilon_3\eta) & 1-2(\varepsilon_3^2+\varepsilon_1^2) & 2(\varepsilon_2\varepsilon_3+\varepsilon_1\eta) \\ 2(\varepsilon_3\varepsilon_1+\varepsilon_2\eta) & 2(\varepsilon_3\varepsilon_2-\varepsilon_1\eta) & 1-2(\varepsilon_1^2+\varepsilon_2^2) \end{pmatrix}. \tag{7}$$

The time evolution of the rotation is expressed by Euler's quaternions, as follows:

$$\begin{pmatrix} \mathrm{d}\varepsilon_1/\mathrm{d}t \\ \mathrm{d}\varepsilon_2/\mathrm{d}t \\ \mathrm{d}\varepsilon_3/\mathrm{d}t \\ \mathrm{d}\eta/\mathrm{d}t \end{pmatrix} = \frac{1}{2}\begin{pmatrix} \eta\omega_{x''} - \varepsilon_3\omega_{y''} + \varepsilon_2\omega_{z''} \\ \varepsilon_3\omega_{x''} + \eta\omega_{y''} - \varepsilon_1\omega_{z''} \\ -\varepsilon_2\omega_{x''} + \varepsilon_1\omega_{y''} + \eta\omega_{z''} \\ -\varepsilon_1\omega_{x''} - \varepsilon_2\omega_{y''} - \varepsilon_3\omega_{z''} \end{pmatrix}, \tag{8}$$

where ω_i, $i = x'', y'', z''$, denotes the spatial component of the angular velocity $\vec{\omega}$.

The governing equation for the translatory motion is

$$m_p\frac{\mathrm{d}\vec{v}}{\mathrm{d}t} = m_p\vec{g} + \vec{F}_D + \vec{F}_L, \tag{9}$$

where $\vec{v}$ is the velocity of the mass center of fiber, $\vec{g}$ the gravitational acceleration, $\vec{F}_D$ the hydrodynamic drag force, $\vec{F}_L$ the shear-induced lift force and m_p is the mass of the fiber given by

$$m_p = \frac{4}{3}\pi a b^2 \rho_p. \tag{10}$$

Here, ρ_p denotes the fiber density, a the semi-major particle axis, and b the semi-minor particle axis. Because of the fiber dimensions and the flow regime considered in this study, other forces, such as the Brownian force and virtual mass force, were neglected.

The equations governing the rotation are

$$\begin{aligned} I_{x''}\frac{\mathrm{d}\omega_{x''}}{\mathrm{d}t} - \omega_{y''}\omega_{z''}(I_{y''} - I_{z''}) &= T_{x''} \\ I_{y''}\frac{\mathrm{d}\omega_{y''}}{\mathrm{d}t} - \omega_{x''}\omega_{z''}(I_{z''} - I_{x''}) &= T_{y''} \\ I_{z''}\frac{\mathrm{d}\omega_{z''}}{\mathrm{d}t} - \omega_{y''}\omega_{x''}(I_{x''} - I_{y''}) &= T_{z''}, \end{aligned} \tag{11}$$

I_i are the spatial components of the moment of inertia matrix in the particle frame of reference:

$$I_{x''} = I_{y''} = \frac{4\pi}{15}\beta(\beta^2+1)b^5\rho_p, \quad I_{z''} = \frac{8\pi}{15}b^5\rho_p. \tag{12}$$

This coordinate system coincides with the principal axis of the spheroid, and the non-diagonal elements in $\mathbf{I}$ are zero, which simplifies Eq. (11). T_i are the spatial components of the hydrodynamic torque acting on the fiber and $\beta = a/b$ is the aspect ratio.

The hydrodynamic drag force $\vec{F}_D$ is computed using the expression by Brenner [64] valid for Stokes flows:

$$\vec{F}_D = \mu\pi b\mathbf{K}'(\vec{u} - \vec{v}), \tag{13}$$

where μ is the fluid dynamic viscosity, $\vec{u}$ the velocity vector of the fluid in the particle mass center and

$$\mathbf{K}' = \mathbf{A}^{-1}\mathbf{K}''\mathbf{A} \tag{14}$$

are the translational dyadics — a diagonal matrix of correction factors depending on the aspect ratio:

$$K''_{xx} = K''_{yy} = \frac{16\left(\beta^2-1\right)}{\left[\left(2\beta^2-3\right)\ln\left(\beta+\sqrt{\beta^2-1}\right)/\sqrt{\beta^2-1}\right]+\beta}, \tag{15}$$

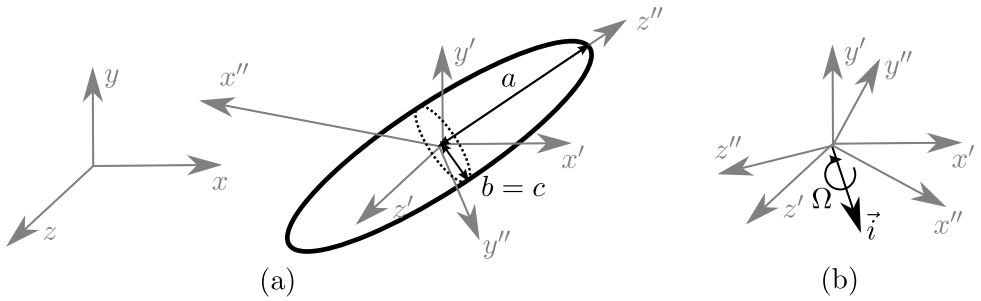

Fig. 4. (a) Approximation of a fiber as a prolate spheroid with the corresponding coordinate systems: the laboratory frame of reference (xyz), the particle co-moving frame of reference ($x'y'z'$), and the particle frame of reference ($x''y''z''$). (b) Illustration of fiber rotation using a quaternion.

$$K''_{zz} = \frac{8\left(\beta^2-1\right)}{\left[\left(2\beta^2-1\right)\ln\left(\beta+\sqrt{\beta^2-1}\right)/\sqrt{\beta^2-1}\right]-\beta}. \tag{16}$$

The shear-induced lift force ($\vec{F}_L$) for a linear shear flow was originally derived by Harper and Chang [65] for a one-dimensional flow, and later extended to arbitrary flows by Cui et al. [66,67]. This force is included in our model under the assumption that the particles are sufficiently small that the flow field can be linearly approximated in their vicinity.

$$\vec{F}_L = \pi^2\rho_f\sqrt{\nu}b^2\vec{l} \tag{17}$$

with

$$\begin{aligned}\vec{l} =& \left(\frac{\partial u_x/\partial y}{\left|\partial u_x/\partial y\right|^{1/2}}\mathbf{K}'\cdot\mathbf{L}_{xy}\cdot\mathbf{K}' + \frac{\partial u_x/\partial z}{\left|\partial u_x/\partial z\right|^{1/2}}\mathbf{K}'\cdot\mathbf{L}_{xz}\cdot\mathbf{K}'\right)\cdot\begin{pmatrix}u_x-v_x\\-v_y\\-v_z\end{pmatrix}+\\ &\left(\frac{\partial u_y/\partial x}{\left|\partial u_y/\partial x\right|^{1/2}}\mathbf{K}'\cdot\mathbf{L}_{yx}\cdot\mathbf{K}' + \frac{\partial u_y/\partial z}{\left|\partial u_y/\partial z\right|^{1/2}}\mathbf{K}'\cdot\mathbf{L}_{yz}\cdot\mathbf{K}'\right)\cdot\begin{pmatrix}-v_x\\u_y-v_y\\-v_z\end{pmatrix}+\\ &\left(\frac{\partial u_z/\partial x}{\left|\partial u_z/\partial x\right|^{1/2}}\mathbf{K}'\cdot\mathbf{L}_{zx}\cdot\mathbf{K}' + \frac{\partial u_z/\partial y}{\left|\partial u_z/\partial y\right|^{1/2}}\mathbf{K}'\cdot\mathbf{L}_{zy}\cdot\mathbf{K}'\right)\cdot\begin{pmatrix}-v_x\\-v_y\\u_z-v_z\end{pmatrix}.\end{aligned} \tag{18}$$

$\mathbf{L}_{ij}$ are permutations of the lift tensor

$$\begin{aligned}\mathbf{L}_{xy} &= \begin{pmatrix}A&B&0\\D&E&0\\0&0&C\end{pmatrix}, \quad \mathbf{L}_{xz} = \begin{pmatrix}A&0&B\\0&C&0\\D&0&E\end{pmatrix},\\ \mathbf{L}_{yx} &= \begin{pmatrix}E&D&0\\B&A&0\\0&0&C\end{pmatrix}, \quad \mathbf{L}_{yz} = \begin{pmatrix}C&0&0\\0&A&B\\0&D&E\end{pmatrix},\\ \mathbf{L}_{zx} &= \begin{pmatrix}E&0&D\\0&C&0\\B&0&A\end{pmatrix}, \quad \mathbf{L}_{zy} = \begin{pmatrix}C&0&0\\0&E&D\\0&B&A\end{pmatrix},\end{aligned} \tag{19}$$

with

$$A = 0.0501, B = 0.0329, C = 0.0373, D = 0.0182, E = 0.0173. \tag{20}$$

The hydrodynamic torque is given by the following expressions proposed by Jeffery [68]:

$$\begin{aligned}T_{x''} &= \frac{16\pi\mu b^3\beta}{3(\beta_0+\beta^2\gamma_0)}\Big((1-\beta^2)D_{z''y''}+(1+\beta^2)(W_{z''y''}-\omega_{x''})\Big),\\ T_{y''} &= \frac{16\pi\mu b^3\beta}{3(\alpha_0+\beta^2\gamma_0)}\Big((-1+\beta^2)D_{x''z''}+(1+\beta^2)(W_{x''z''}-\omega_{y''})\Big),\\ T_{z''} &= \frac{32\pi\mu b^3\beta}{3(\alpha_0+\beta_0)}(W_{y''x''}-\omega_{z''}),\end{aligned} \tag{21}$$

where

$$D_{ij} = \frac{1}{2}\left(\frac{\partial u_i}{\partial x_j}+\frac{\partial u_j}{\partial x_i}\right) \tag{22}$$

are the components of the deformation rate tensor and

$$W_{ij} = \frac{1}{2}\left(\frac{\partial u_i}{\partial x_j}-\frac{\partial u_j}{\partial x_i}\right) \tag{23}$$

are the components of the spin-rate tensor, both in the particle frame of reference. The non-dimensional coefficients α_0, β_0 and γ_0 are defined as follows:

$$\begin{aligned}\alpha_0 = \beta_0 &= \frac{\beta^2}{\beta^2-1}+\frac{\beta}{2(\beta^2-1)^{3/2}}\ln\frac{\beta-\sqrt{\beta^2-1}}{\beta+\sqrt{\beta^2-1}},\\ \gamma_0 &= -\frac{2}{\beta^2-1}+\frac{\beta}{(\beta^2-1)^{3/2}}\ln\frac{\beta-\sqrt{\beta^2-1}}{\beta+\sqrt{\beta^2-1}}.\end{aligned} \tag{24}$$

Here, again, the assumption of linear shear flow around the particle was used.

The translational and rotational motions of the fibers were coupled. First, the particle position and angular velocities were updated by solving Eqs. (9) and (11). Then, the time rate of change of the orientation is determined using Euler quaternions by solving Eq. (8). This allows computation of the updated orientation. Finally, the orientation vector of the major axis was obtained by multiplying the transformation matrix **A** from (7).

Deposition mechanisms. The nonspherical shape of the fibers introduces a new deposition mechanism compared to spherical particles: interception. In particular, long fibers may contact the airway wall with their tips. Therefore, deposition depends on the orientation of the fiber. To model this, a boundary condition is prescribed, where every particle–wall contact results in particle deposition. In each iteration, the algorithm checks for potential wall contact by calculating the distance d_s from the center of mass of the fiber to the closest point on the nearest triangle of the STL geometry. The following three scenarios are possible.

1. $d_s > a$, the distance is greater than the semi-major axis, and no deposition occurs.
2. $d_s < b$, the distance is less than the semi-minor axis, and the particle is deposited.
3. $b < d_s < a$, deposition depends on the orientation, and further treatment is required.

In Case 3, the exact particle orientation must be considered. Fan and Ahmadi proposed an algorithm for this [69] and later Tian et al. [27,39] applied it. This algorithm is rarely described step-by-step, and is thus presented here.

The goal is to rotate the particle coordinate system ($x''y''z''$) such that the new wall-local coordinate system ($x_wy_wz_w$) is aligned parallel to the wall, which is represented by the STL-triangle. The inclination angle (α) between the coordinate systems is calculated from the STL-triangle normal vector ($\vec{n_w}$) and the semi-major particle axis vector ($\vec{n_p}$), as shown in Fig. 5, using the inner product

$$\alpha = \arccos\left(\frac{\vec{n}_w\cdot\vec{n}_p}{|\vec{n}_w||\vec{n}_p|}\right) \tag{25}$$

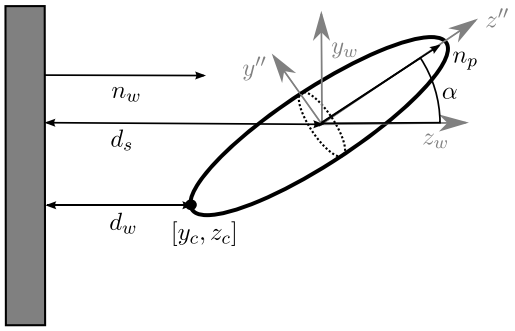

Fig. 5. Visualization of the fiber deposition process, illustrating the determination of the closest point on the fiber surface to the airway wall to assess potential contact and deposition.

Owing to the rotational symmetry of the spheroids, the problem can be simplified by projecting it into 2D. The projected spheroid forms an ellipse, which is given by the following equation in the particle frame of reference:

$$\frac{y''^2}{b^2} + \frac{z''^2}{a^2} = 1. \tag{26}$$

In the wall reference, using the 2D rotational transformation

$$\begin{aligned} y'' &= y_w \cos\alpha - z_w \sin\alpha, \\ z'' &= y_w \sin\alpha + z_w \cos\alpha, \end{aligned} \tag{27}$$

the ellipse is expressed as follows:

$$\frac{(y_w \cos\alpha - z_w \sin\alpha)^2}{b^2} + \frac{(y_w \sin\alpha + z_w \cos\alpha)^2}{a^2} = 1. \tag{28}$$

The lower part of the ellipse, including the point closest to the wall, was determined using the following relation:

$$y_w = \frac{-ab\sqrt{a^2\cos^2\alpha + b^2\sin^2\alpha - z_w^2} + z_w \sin\alpha\cos\alpha(b^2 - a^2)}{a^2\cos^2\alpha + b^2\sin^2\alpha}. \tag{29}$$

The point closest to the wall is determined by setting the derivative of z_w with respect to y_w to zero:

$$\frac{\mathrm{d}z_w}{\mathrm{d}y_w} = 0, \tag{30}$$

from which the z_c coordinate is

$$z_c = \sin\alpha\cos\alpha(b^2 - a^2)\sqrt{\frac{(a^2\cos^2\alpha + b^2\sin^2\alpha)}{a^2b^2 + \sin^2\alpha\cos^2\alpha(b^2 - a^2)^2}}. \tag{31}$$

Note that the positive root was considered according to particle orientation. Inserting z_c into Eq. (29) returns the second coordinate (y_c) of the point closest to the wall:

$$y_c = \frac{-ab\sqrt{a^2\cos^2\alpha + b^2\sin^2\alpha - z_c^2} + z_c \sin\alpha\cos\alpha(b^2 - a^2)}{a^2\cos^2\alpha + b^2\sin^2\alpha}. \tag{32}$$

If $|z_c| > d_s$, then this point lies inside the wall and the particle is deposited. If $|z_c| < d_s$, then the closest point is inside the geometry and no deposition occurs. The absolute value of z_c accounts for both possible particle orientations (i.e., both the positive and negative roots in Eq. (31)).

The computation of the particle trajectories is coupled with the fluid field through the fluid velocity ($\vec{u}$) at the center of mass of each particle. This velocity is used to compute the forces (Eqs. (13) and (17)) and torque (Eq. (21)). The complete numerical procedure is shown in Fig. 6.

In total, 50,000 homogeneous particles ($\rho_p = 2650\ \mathrm{kg\,m^{-3}}$) were released during the first inspiration cycle in the simulation. The dimensions of the fibers were obtained from the log-normal distribution of all particles measured in the deposition experiment: $a = 7.96 \pm 5.09$ µm and $b = c = 0.83 \pm 0.47$ µm. The initial position of each particle is randomly generated from a uniform distribution within a circle near the mouth inlet. The initial orientation was randomly generated. Experimentally, it is impossible to determine the exact position, velocity, and orientation of each fiber entering the geometry. To represent the gradual inhalation of particles, the particles were not released simultaneously. Instead, they were released in batches distributed over 100 discrete time steps within the inspiration cycle. The number of particles released at each time step was proportional to the actual flow rate at that time (see Fig. 3), reflecting the fact that a higher flow rate carries more particles into the airway.

The numerical simulations were performed using the open-source C++ library OpenLB [70–72]. This software enables flexible and performant simulations using the LBM, benefiting from efficient parallelization and scalability of both CPUs and GPUs on high-performance computers. The suitability of OpenLB for this type of application was demonstrated in a previous paper by the authors [41], which resulted in high performance and accuracy. To simulate fiber transport and deposition, OpenLB was extended using an integrated in-house code that implemented the ELER model. The simulations were performed on the Karolina supercomputer petascale system at the IT4Innovation National Computing Center in Czechia using 1024 CPU cores distributed across multiple nodes, leveraging the high memory capacity and interconnect bandwidth of the HPC system.

For comparison with experimental results, the following statistical quantities were evaluated:

Deposition fraction

$$\mathrm{DF} = \frac{N_s}{N_{tot}}, \tag{33}$$

where N_s is the number of particles deposited in a given segment, and N_{tot} is the total number of particles entering the geometry.

The deposition efficiency DE describes the efficiency of a segment in capturing the particles.

$$\mathrm{DE} = \frac{N_s}{N_{s,in}}, \tag{34}$$

where $N_{s,in}$ is the number of particles entering the segment.

Volume equivalent diameter

$$d_{eq} = \sqrt[3]{\frac{6V}{\pi}}, \tag{35}$$

is defined as the diameter of the spherical particle having the same volume as the fiber.

Aerodynamic diameter

$$d_{ae} = d_{eq}\sqrt{\frac{\rho_p}{\rho_0 \chi_R}} \tag{36}$$

is defined as the diameter of a sphere with unit density (ρ_0) that settles with the same terminal velocity as the fiber. χ_R denotes the dynamic shape factor for a random orientation.

The Stokes number, given by

$$\mathrm{Stk} = \frac{\rho_0 d_{ae}^2 u_0}{18\mu D_0}, \tag{37}$$

is an important dimensionless parameter for evaluating the rate of the inertial impaction. It is particularly useful for comparing data across different flow rates and geometries because it accounts for the combined effects of particle inertia, fluid viscosity, and characteristic length scales. In this equation, u_0 represents the characteristic velocity of the flow, and D_0 represents the characteristic dimension of the geometry.

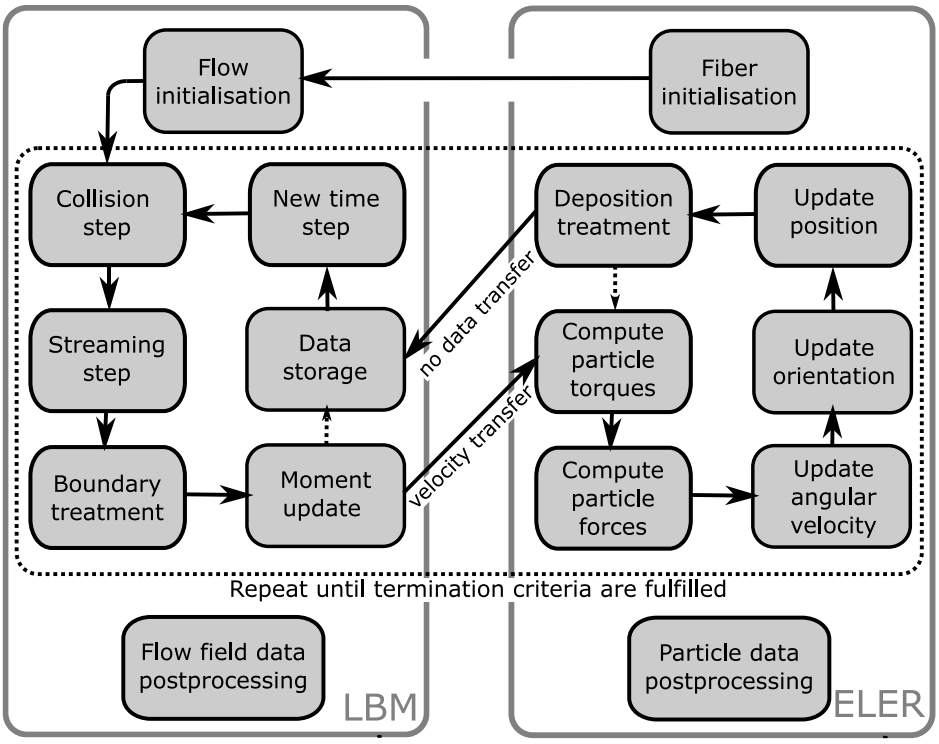

Fig. 6. Schematic of the numerical setup. After the initialization step, each iteration involves one LBM cycle and one ELER cycle. After computing the flow velocities (u) in the LBM cycle, these values are transferred to the ELER algorithm. Due to the one-way coupling, no data are transferred back from the ELER algorithm to the LBM solver. In principle, different numbers of LBM or ELER cycles can be performed within each iteration (e.g., inner iterations), as indicated by the dotted arrows. The simulation terminates when the specified criteria (e.g., simulation time or number of iterations) are met, and the data are then post-processed.

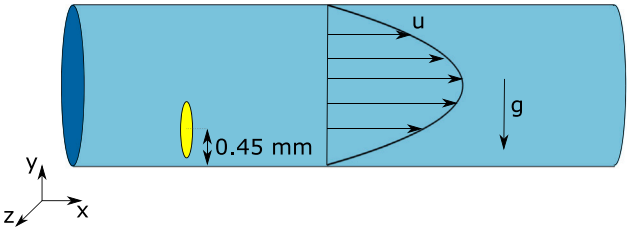

Fig. 7. Initial condition of the fiber in the numerical verification case, showing its position and orientation relative to the airflow in the horizontal pipe.

2.3. Numerical verification

Verification of the ELER method implementation within the LBM framework was performed using a benchmark case of laminar airflow through a circular tube. This benchmark, often with small variations, has been used for verification in several studies [13,27,73–75]. In this paper, the specific setup first described by Tian et al. [27] was simulated, and data from Feng et al. [13] were also used for comparison. This involved simulating laminar flow through a horizontal pipe with a diameter of 4.2 mm and a corresponding Reynolds number of Re = 169. A spheroidal particle with a minor axis of 0.5 μm and an aspect ratio of 14 was injected at a position 0.45 mm above the bottom edge of the pipe, with an initial perpendicular orientation. The particle trajectory was then tracked for 0.2 s (see Fig. 7).

To compare the results of our simulation with those of Tian et al. [27] and Feng et al. [13], the directional cosines between the fiber symmetry axis and the coordinate axes were evaluated. The time evolution of these quantities over 0.2 s of the simulation is shown in Figs. 8(a) and 8(b). As can be seen, the fiber quickly tilts from its initial perpendicular orientation to a position parallel to the flow. After each period of 0.055 s, it undergoes a 180-degree flip.

The sedimentation velocity, shown in Fig. 8(c), was also compared. Gravity acts on the fiber, causing it to move in the negative y direction. The sedimentation velocity increases from zero to a terminal velocity, at which point the gravitational force is balanced by drag force. When the fiber flips from a parallel to a perpendicular orientation, its cross-sectional area decreases, leading to a reduction in the drag force and sudden acceleration.

To demonstrate a more robust comparison, the trajectory of the particle in the moving xy plane was plotted and compared (see Fig. 9). The particle is driven predominantly in the fluid direction, while gravity governs a slow downward shift.

In all cases, the close agreement between our results and those of Tian et al. and Feng et al. demonstrates the correctness of our implementation of the ELER method. The discrepancies may be attributed to differences in numerical setup — the case depends on the viscosity and density of the fluid which are not stated in any of the aforementioned studies. Furthermore, as previously reported by Cui et al. [74], the frequency of flips depends on the Re, which slightly varies between the studies. Different numerical discretization schemes or discrepancies in the lift force formulations can also contribute to variations [13].

2.4. Grid independence study

To assess the validity of the numerical simulations and ensure that the results were not significantly influenced by grid resolution, a grid-independence study was conducted. The grid size was initially chosen based on a previous study [41], which used the same rescaled realistic geometry.

To evaluate grid independence, line probes were placed downstream of the first bifurcation near the carina, with two probes in the anterior direction and two in the superior direction (see Fig. 11(a)). This area is characterized by turbulent flow conditions, making it suitable for assessing the impact of grid resolution on flow features. A time period of 0.1 s was simulated with a constant flow rate corresponding to the

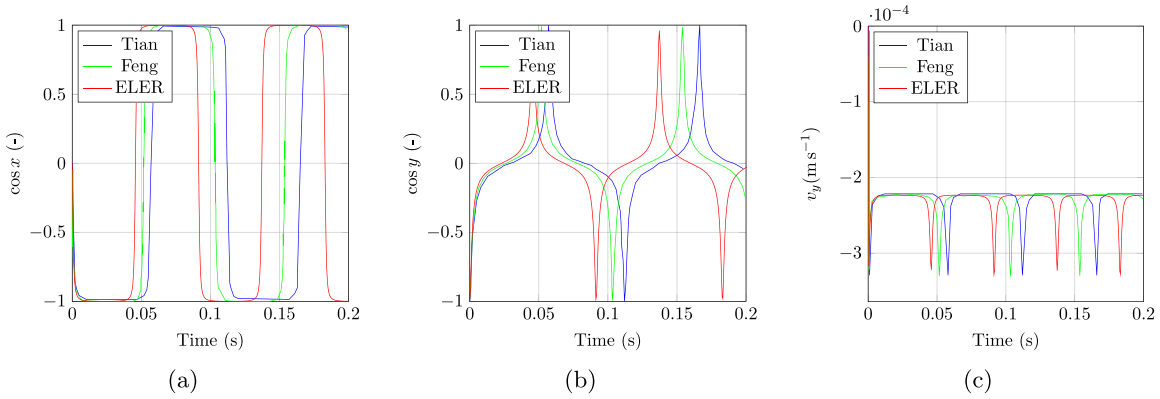

Fig. 8. Comparison of the time evolution of (a) the directional cosine between the symmetry axis of a fiber and the x-axis ($\cos x$), (b) the directional cosine between the symmetry axis of a fiber and the y-axis ($\cos y$), and (c) the sedimentation velocity (v_y) obtained in this study with the results reported by Tian et al. [27]. and Feng et al. [13].

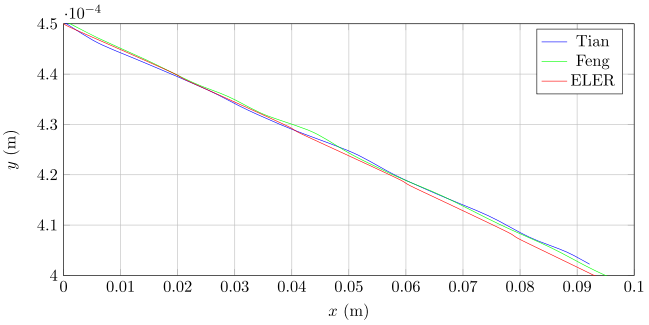

Fig. 9. Comparison of the fibers centroid trajectory with the results reported by Tian et al. [27] and Feng et al. [13].

Table 1
Properties of lattices used for the grid independence study.

Number of cells	Cell size	Time step	Relaxation time
40 mil.	0.00018 m	$3.5.10^{-7}$ s	0.5005
60 mil.	0.00015 m	$2.6.10^{-7}$ s	0.5005
82 mil.	0.00013 m	$2.0.10^{-7}$ s	0.5005

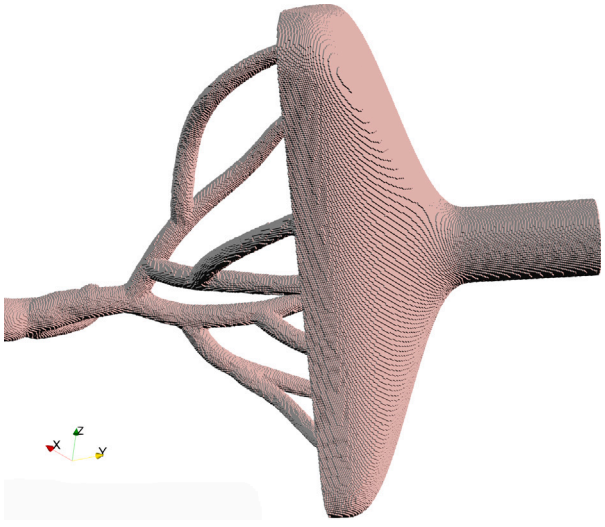

Fig. 10. Detail of the computational grid of the right upper lobe (RUL).

peak flow rate of the inspiratory cycle (27 $1\,\mathrm{min}^{-1}$). This flow rate was chosen because the numerical errors tend to be the highest at the maximum fluid velocity. The mean velocity magnitude along the line probes was used for comparison to minimize the influence of local fluctuations.

Three different grids with a uniform grid size (for details, see Table 1 and Fig. 10) were simulated, and the results are shown in Fig. 11(b)–(e). Good agreement in the mean velocity magnitude was observed between the grids with 60 million and 82 million cells. The final simulation was performed using an intermediate grid of 60 million cells.

2.5. Effective diameter simulations

The effective diameter simulations are simplified Euler–Lagrange simulations, where the particles are approximated by spheres and the rotation (Eq. (11)) is neglected. To establish an accurate comparison of ELER with this method, two additional simulations with the most popular empirical models, H–L [22] and T-C [21], on the same geometry under the same breathing conditions were conducted. The hydrodynamic drag force is defined as

$$\vec{F}_D = \frac{1}{2} C_D A_p \rho_p (\vec{u} - \vec{v}) |\vec{u} - \vec{v}| \tag{38}$$

where A_p is the projected surface area, and C_D is the hydrodynamic shape factor.

In the H–L correlation, the C_D is determined as

$$C_D = \frac{24}{\mathrm{Re}_p}(1 + H_a \mathrm{Re}_p^{H_b}) + \frac{H_c \mathrm{Re}_p}{H_d + \mathrm{Re}_p}, \tag{39}$$

where

$$\mathrm{Re}_p = \frac{|\vec{u} - \vec{v}| d_p}{\nu} \tag{40}$$

is the Reynolds number of the particle. ν denotes the fluid kinematic viscosity, and H_a, H_b, H_c and H_d are model-specific parameters that depend on particle sphericity ϕ.

T-C defines the shape factor as follows.

$$C_D = \frac{24}{\mathrm{Re}_p} \frac{d_A}{d_{eq}} \left(1 + \frac{0.15}{\sqrt{c}} \left(\frac{d_A}{d_{eq}} \mathrm{Re}_p\right)^{0.687}\right) + \frac{0.42 \left(\frac{d_A}{d_{eq}}\right)^2}{\sqrt{c}\left(1 + 42500 \left(\frac{d_A}{d_{eq}} \mathrm{Re}_p\right)^{-1.16}\right)}, \tag{41}$$

where d_A is the surface equivalent sphere diameter, and c is the surface sphericity.

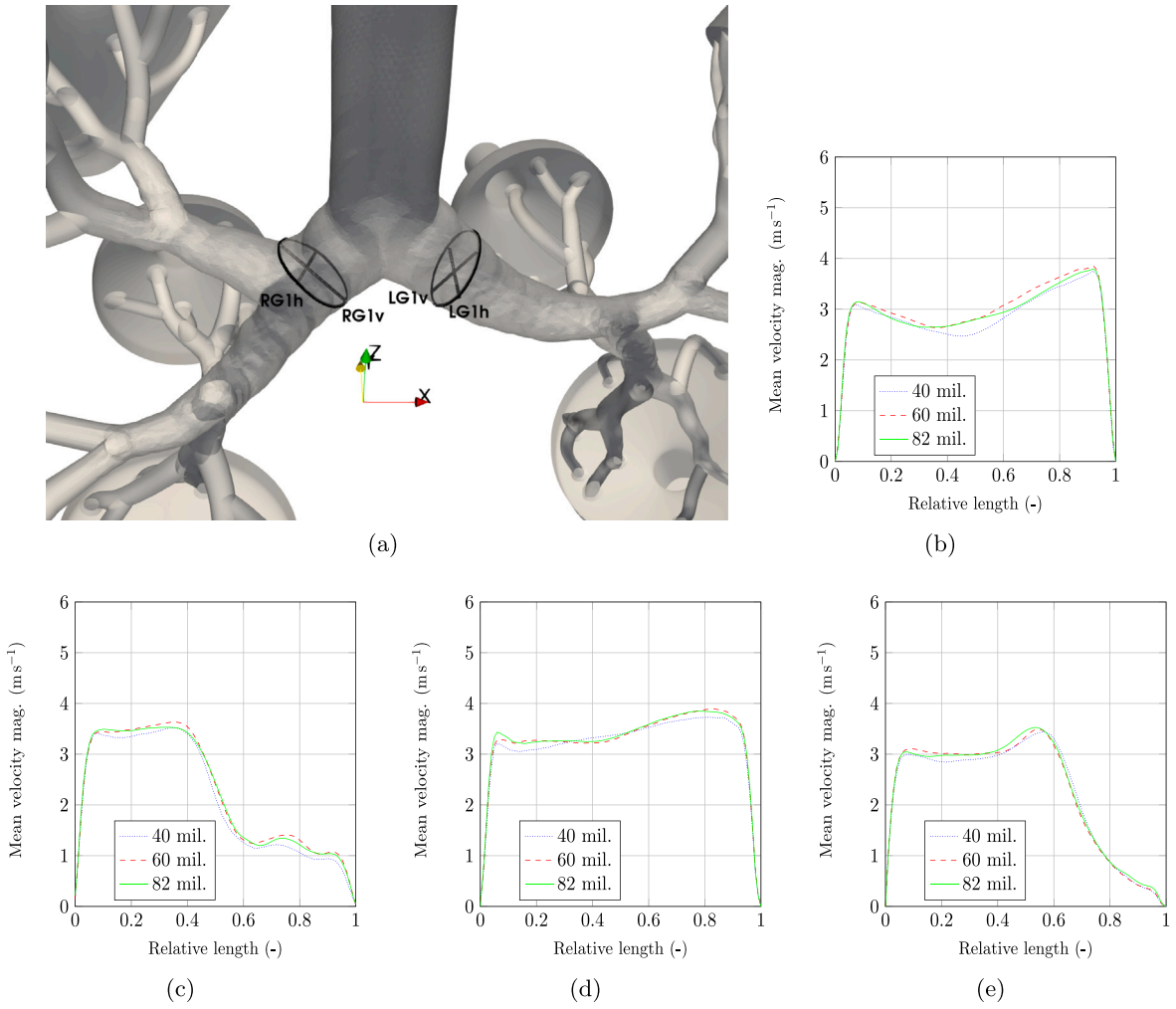

Fig. 11. Grid independence study: (a) Locations of the line probes used to assess grid independence, (b)–(e) mean velocity magnitude along the line probes for three different grid resolutions; (b) Left branch, horizontal probe (LG1h), (c) Left branch, vertical probe (LG1v), (d) Right branch, horizontal probe (RG1h), (e) Right branch, vertical probe (RG1v).

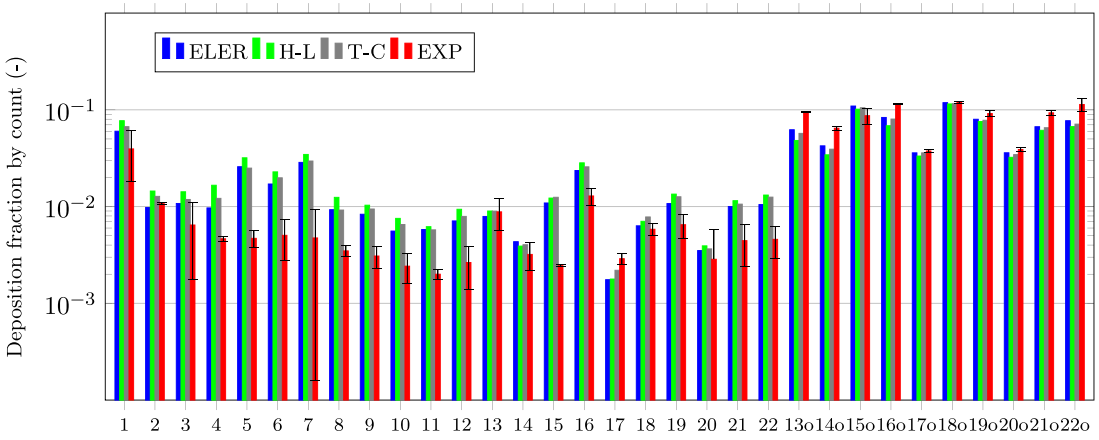

Fig. 12. Comparison of deposition fractions obtained from experimental measurements and numerical simulations.

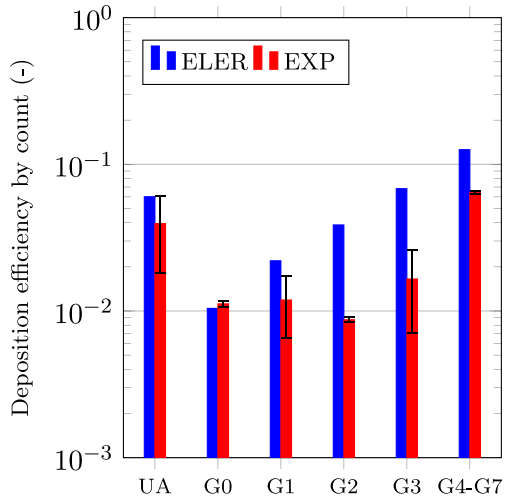

Fig. 13. Comparison of deposition efficiencies obtained from experimental measurements and numerical simulations, sorted by airway generation.

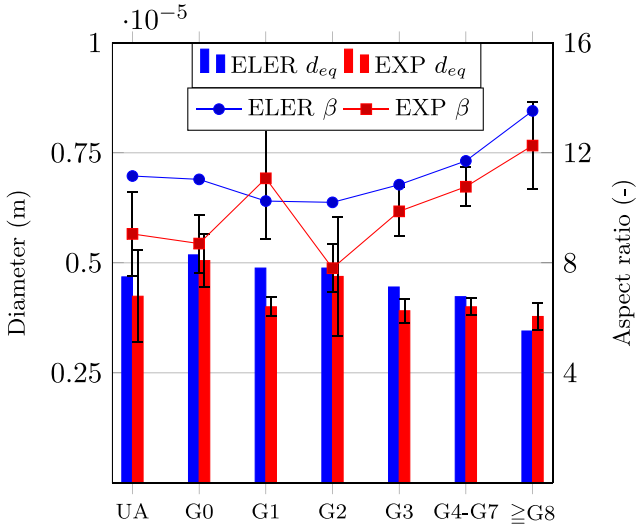

Fig. 14. Comparison of the mean equivalent diameter (d_{eq}) and mean aspect ratio (β) of deposited fibers for each airway generation. The bar chart (left vertical axis) shows the mean equivalent diameter, while the symbols (right vertical axis) show the mean aspect ratio.

3. Results and discussion

3.1. Comparison between simulation and experiment

Fig. 12 compares the numerical and experimental results for the fiber deposition. The simulation data were analyzed at the end of the simulation, and approximately 5% of the particles that had not yet been deposited were excluded from the evaluation. In many segments, good agreement was observed between the simulation and the experiment, particularly in the segments above the bifurcations (segments 1, 2, and 3) and at the funnels at the outlets (segments 13o-22o). Numerical simulation generally predicts a slightly higher deposition fraction in most bifurcations. This discrepancy can be attributed partly to differences in the deposition mechanisms and surface interactions. In the LBM simulations, every contact between a particle and the wall resulted in deposition (the 'perfect sink' assumption). While the experimental replica surface was coated with silicone oil to promote adhesion and mimic mucus capture [16,17], the simulation's assumption of 100% capture upon any contact might still represent an upper bound compared to the in vitro reality, potentially contributing to the observed overestimation. Further investigation of particle–wall interactions under varying surface conditions is necessary to improve the accuracy of the deposition model. Another source of discrepancies may stem from assumptions of linear shear flow in the force calculation. This assumption might result in discrepancies in the areas of the bifurcations [76]. In addition, the periodic rotational motion of the particles, which is assumed in the ELER method, is not consistently observed in experiments, as reported by Lizal et al. [18]. The largest differences between the simulation and experiment occurred in segments 5, 6, and 7, which corresponded to the second and third generations of branching in the left lung. This excess deposition in the simulation is likely compensated for by a consequent lower deposition fraction in the downstream segments (13, 13o, 16o, 17, 17o), where the experimental results show higher values. The numerical results for the right lung were in good agreement with the experimental data. A further statistics of the experimental data, specifically on counts and dimensions of fibers deposited in each segment can be found in Table A.2 in Appendix.

To further assess the accuracy of the numerical simulations, a comparison was made between the ELER method and two simplified models based on the effective diameter concept: the T-C model [22] and H–L model [21]. These models approximate the fibers as spheres with equivalent diameters and neglect their rotation. Analysis of the results revealed that the ELER model provided the most accurate predictions of deposition, with the best agreement with the experimental data in 26 segments, compared to five segments for the T-C model and only two segments for the H–L model. The absolute errors for the ELER, T-C, and H–L models were 0.0106, 0.0120, and 0.0146, respectively, confirming the superior accuracy of the ELER approach. This finding is consistent with H–L and T-C comparison studies by Farkas [25]. Based on these results, only the ELER simulation results were considered in the subsequent analysis and discussion.

The deposition parameters were analyzed as a function of airway generation to provide a comparison relevant to medical applications. Each segment was assigned its highest generation number, as shown in Fig. 2. The deposition fraction and efficiency were then calculated for the following regions: upper airway (UA); trachea (generation 0, G0); generations G1, G2, and G3; and generations G4-G7. Generations G4-G7 were grouped together because these higher-generation segments are manufactured as single pieces due to their small dimensions.

Fig. 13 shows the deposition efficiency of each generation. The deposition efficiency generally increased with increasing generation order in both the simulation and experiment, with a steeper increase observed in the LBM results. However, in the experimental results, G2 deviated from this trend, showing a decrease in deposition efficiency compared to G1. Larger discrepancies between the simulation and experiment were observed for the higher generations of branching.

The experimental setup used in this study allowed for a unique analysis of the deposition data based on the dimensions of the captured fibers in each segment. This type of analysis is rare in similar experimental studies on fiber deposition. Fig. 14 compares the mean values of the volume equivalent diameter (d_{eq}) and aspect ratio (β) of the deposited fibers in the upper airways and different generations of branching. In both cases, a reasonable agreement was observed between the simulation and experiment.

As expected, particles with higher d_{eq} were predominantly deposited in the upper airways and the first few tracheobronchial generations because of their higher inertia. On the other hand, smaller fibers tend to penetrate deeper into the lungs. This trend was evident in both the experimental and numerical results, although the experimental data exhibited slightly more fluctuations. The largest discrepancies between the simulation and experiment occurred in G1, which could be due to the low number of deposited and measured particles in this segment, leading to a higher statistical error.

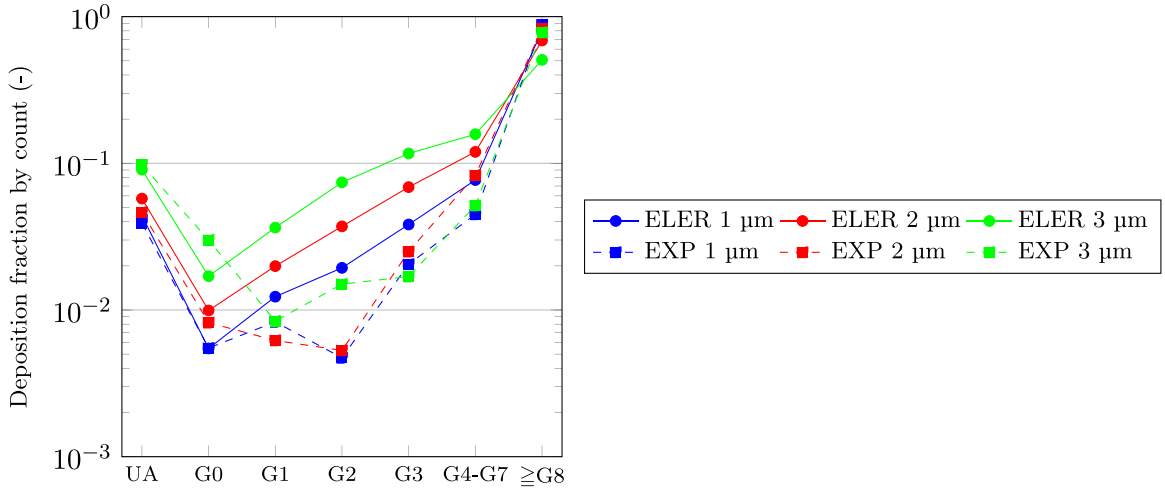

Fig. 15. Comparison of deposition fractions for fibers sorted into three size groups based on their diameter (d_p).

Except for the outlets, the simulations generally predicted a higher mean d_{eq} and β than the experiment. While β increased with increasing generation downstream of the trachea in both the experimental and numerical results, d_{eq} decreased. This observation suggests a complex interplay between the rotational motion of the particles and the tendency of the ELER method to capture particles in bifurcations. However, the flow in the first few bifurcations is turbulent, which makes it challenging to simulate the rotational movements of the fibers accurately. For particles with high β, changes in orientation can significantly alter their trajectory (owing to the dependence of the drag force on the streamwise cross-section, as shown in Eq. (13)). This can lead to differences in the deposition patterns between the simulation and the experiment, particularly for larger particles. This is consistent with the observation that the mean d_{eq} of the particles passing through the geometry (i.e., ≥G8) was higher in the experimental setup. A similar behavior was reported by Shachar-Berman et al. [8]. Again, a slight deviation from this trend was observed at G1 in the experiment, likely due to the low number of deposited fibers and the resulting higher statistical error.

A similar trend can be observed in Fig. 15, which shows the deposition fraction for the fibers sorted into three classes according to their thickness ($d_p = 2b = 2c$). For small particles ($d_p = 1$ µm and $d_p = 2$ µm), the upper airway and trachea showed good agreement between the simulation and experimental results. However, larger discrepancies were observed in generations G1, G2, and G3, with the differences increasing with the particle thickness. This is consistent with previous observations that orientation changes have a more significant impact on the trajectories of larger particles. In generations G4-G7, the differences between the simulation and experiment were smaller, which could be attributed to the narrower channels in these regions and the transition back to a laminar flow regime.

Interestingly, these results differ from those of a previous study using an LBM [41] that simulated spherical particles in a rescaled child airway geometry. In that study, larger discrepancies between the simulation and the experiment were observed for smaller particles. This highlights the impact of the particle shape on the deposition patterns and the importance of considering the fiber orientation in simulations.

Fig. 16 compares the deposition efficiency obtained in this study with data available in the literature. To facilitate this comparison, the particles were sorted into groups based on their Stokes numbers to ensure statistically relevant sample sizes for each evaluation. The trachea and segments up to the fourth generation of branching were evaluated separately.

To the best of our knowledge, comparable experimental or simulation data for fiber deposition in a realistic female airway geometry are missing. Therefore, we included data from studies using the male airway geometry by Belka et al. [17] and Farkas et al. [25]. Additionally, we included experimental data from Su et al. [16] and Zhou et al. [15], who used different realistic airway geometries, and Myojo and Takaya [10], who used the idealized Weibel lung model A from the third to fourth generation of branching.

Analysis of the data in Fig. 16 reveals good agreement between our results and the experimental data for the trachea (Fig. 16(a)). Discrepancies compared to the simplified T-C and H–L models are negligible in this region, suggesting less complex flow behavior than in deeper generations. In generations 1–3 (Figs. 16(b)–(d)), our simulations predicted a slightly higher deposition efficiency than the experimental data. This difference may be due to the use of a realistic inspiration profile in our simulations, which includes a higher peak velocity that could increase deposition in comparison with studies that used constant flowrates. The differences between the ELER model and simplified models become more pronounced in higher generations, highlighting the importance of considering fiber rotation in the branching regions. It is worth noting that the experimental data from Su et al. [16] have a higher standard deviation, which should be considered when comparing our results. Overall, the ELER simulations tend to overestimate the fiber deposition compared with our experiments, which is consistent with previous findings.

In Generation 4 (Fig. 16(e)), both our experimental and numerical results show higher deposition across the entire Stk range compared to Myojo and Takaya [10]. This discrepancy could be attributed to the use of an idealized geometry and the absence of upstream bifurcations in their model, which does not account for the full flow history. The experiments of Zhou et al. [15] were conducted for higher Stk values; however, extrapolating their data to the lower Stk range would still indicate lower deposition than that observed in our study.

Interestingly, the experimental data from Belka et al. [17] show a lower deposition efficiency for almost all segments and Stk compared to other studies, including the corresponding H–L and T-C simulations performed by Farkas et al. [25]. This discrepancy could be related to differences in the experimental setup or specific characteristics of the airway models used.

In summary, the female airway geometry used in this study appears to result in a slightly higher deposition rate compared to the male airway geometry, with a shift of the capture-efficiency curve towards lower Stk. However, differences in the specific geometries or the use of a transient flow regime may also contribute to the observed differences in the deposition efficiency, and further investigation is needed to fully understand these effects. The comparison between the ELER model and the simplified T-C and H–L models reveals increasing discrepancies

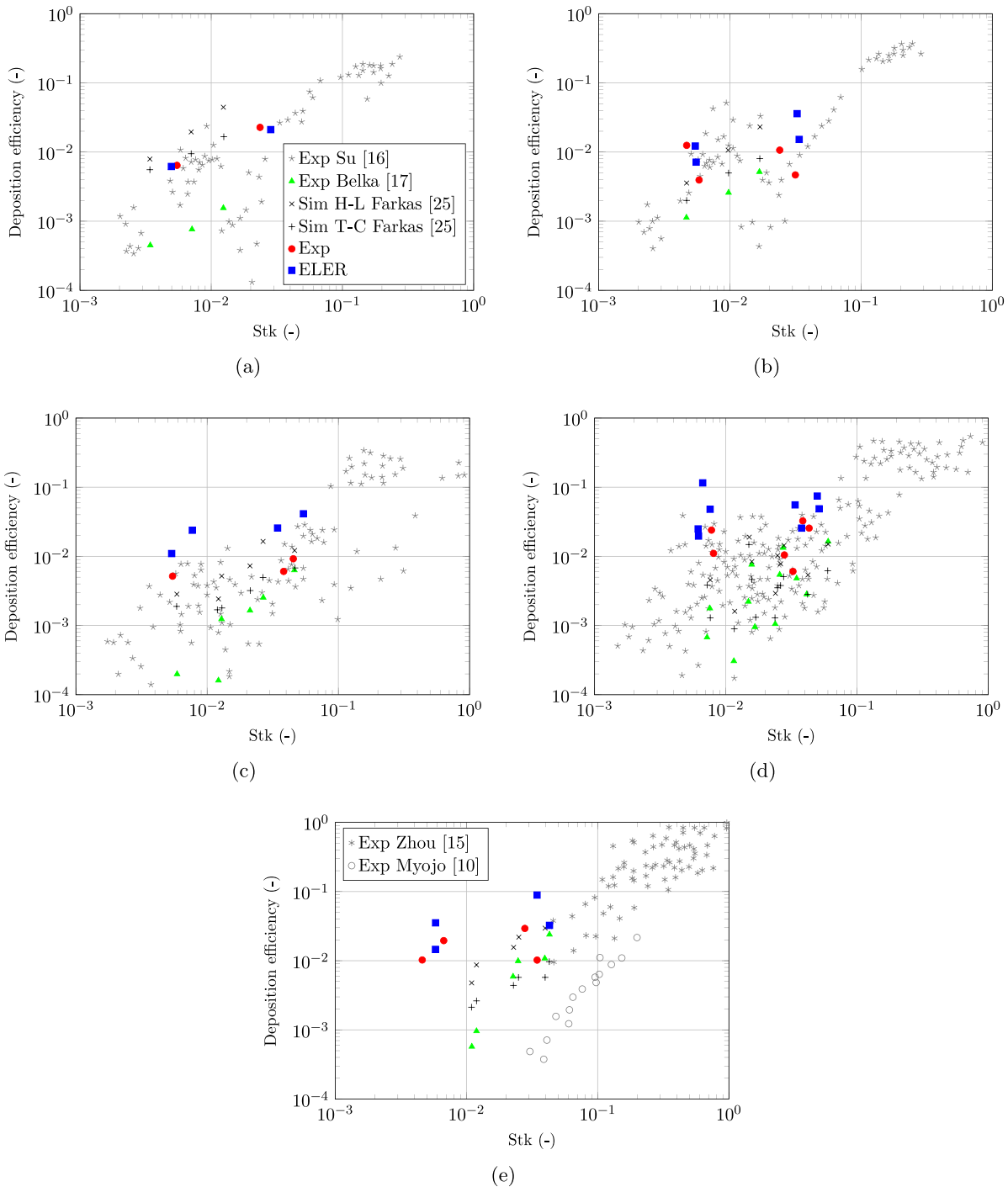

Fig. 16. Comparison of deposition efficiency as a function of Stokes number (Stk) with data from the literature for different airway generations: (a) Trachea, (b) Generation 1, (c) Generation 2, (d) Generation 3, and (e) Generation 4.

with increasing generation number, underscoring the importance of accounting for fiber rotation, especially in deeper airway generations.

3.2. Numerical analysis

The simulation results allow for a more detailed investigation of particle deposition than the experimental results. In Fig. 17, the particle deposition positions based on the aspect ratio can be investigated. The main hotspots are typically located in the oral cavity, larynx and at the carinas of the bifurcations. With increasing airway generation, the flow is more laminar and there are not so many particles to deposit there, as expected. The number of deposited particles grows with the increasing particle diameter leading to a higher Stk. Regarding the aspect ratio, no clear trend regarding preferential deposition locations can be derived as the particles with a higher aspect ratio deposit in the whole geometry with similar concentration. Furthermore, it is very difficult to determine the number of particles deposited in the hotspots based on this visualization.

Therefore, the dependence of deposition efficiency on the aspect ratio β is shown in Fig. 18. To enable comparison of aspect ratio (β) effects among fibers with similar inertial characteristics, the particles were sorted into classes based on their equivalent diameter (d_{eq}). This

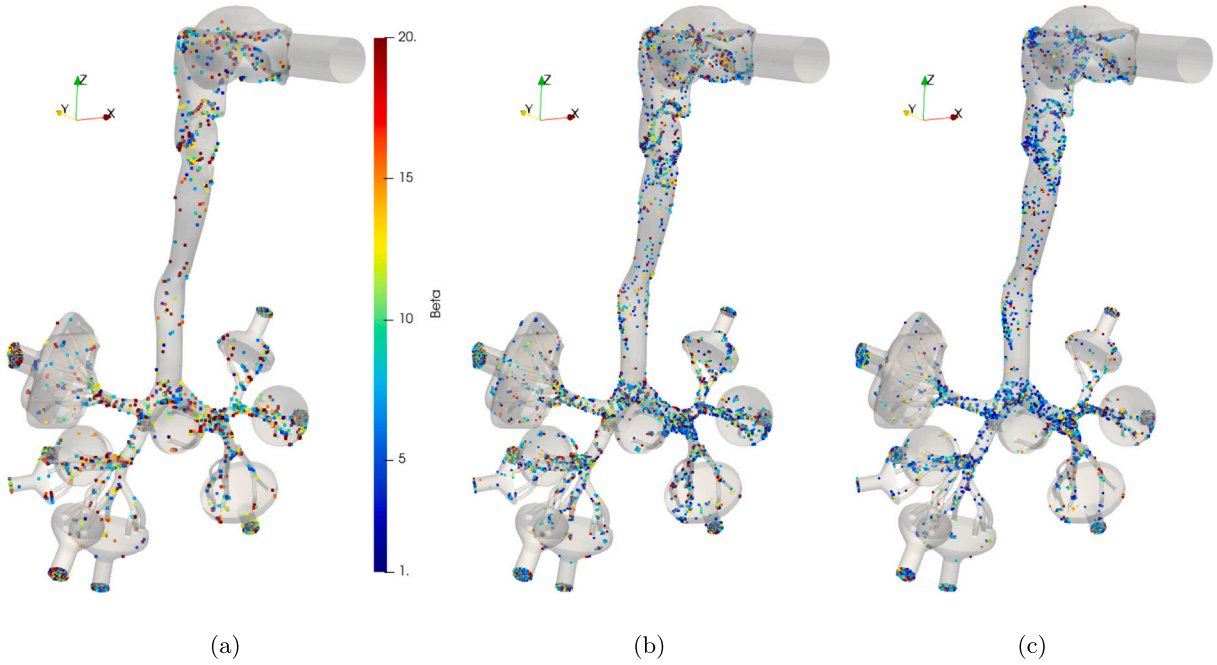

Fig. 17. Visualization of the particle deposition positions in dependence on β for particle equivalent diameter classes (a) below 2.5 μm, (b) 2.5–5 μm and (c) above 5 μm.

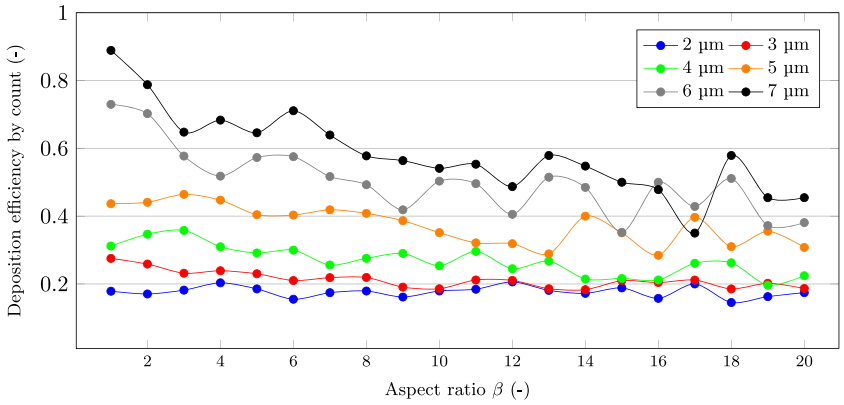

Fig. 18. Comparison of deposition efficiency of the whole geometry in particle classes grouped by d_{eq} in dependence on β.

analysis revealed that the influence of aspect ratio (β) on deposition efficiency is significantly less pronounced for smaller particles (d_{eq}) compared to larger ones. For $d_{eq} = 2$ μm, the deposition efficiency fluctuates at the same level around 0.2 with increasing β. With increasing diameter, the decreasing trend is more significant, mainly for aspect ratios less than 10, for $d_{eq} = 7$ μm, the deposition efficiency falls by 50% from 0.9 for spherical particles ($\beta = 1$) to 0.45 for $\beta = 20$. This is probably caused by the higher cross-section presented by particles oriented perpendicular to the flow, leading to a higher drag force which prevents significant deviation from streamlines. Thus, interception plays a lesser role than the increased drag force in this regime. Greater fluctuations for larger β values result from the decreasing number of particles in the corresponding samples. This emphasizes the importance of considering particle shape in the context of deposition efficiency, which is strongly dependent on particle diameter and the instantaneous flow rate.

Fig. 19 presents a comparison of deposition efficiency of the entire tracheobronchial tree with data by Li et al. [32]. They numerically investigated the deposition of ellipsoidal particles in a realistic geometry of the nasal cavity and tracheobronchial tree of an Asian male under constant breathing rate of 18 $\mathrm{l\,min^{-1}}$. Despite several differences in the setups, these data were the most suitable for the comparison although they modeled a male airway deposition pattern. Here, the deposition efficiency as a function of d_{ae} is visualized. In both studies, a similar trend can be observed. Our results show higher deposition efficiencies for the same d_{ae} and β. This is caused by a higher maximum flow rate of the inspiration profile resulting in higher deposition [77,78]. Further sources of discrepancies are geometric differences between the airway models and the density of the particles. The female geometry has smaller dimensions (higher Stk) resulting in a higher deposition for equal flow rates. Nevertheless, similar to the previous results, the particle aspect ratio has a substantial effect for higher particle sizes.

Furthermore, the influence of the particle release time during the inspiration cycle can be studied, which can provide valuable information for designing inhalation therapies. The flow rate varies throughout the inspiration cycle, subjecting the particles to different flow conditions, potentially leading to different deposition scenarios.

Fig. 20 shows the deposition fraction and d_{eq} for particles sorted according to their release time into three periods: 0–0.2 s, 0.2–0.5 s, and 0.5–1.5 s. Each period contained approximately 15,000 particles. The greatest differences in the deposition fraction were observed in the upper airway. Particles released within the first 0.5 s pass through this region at higher velocities, resulting in a higher Stokes number and thus

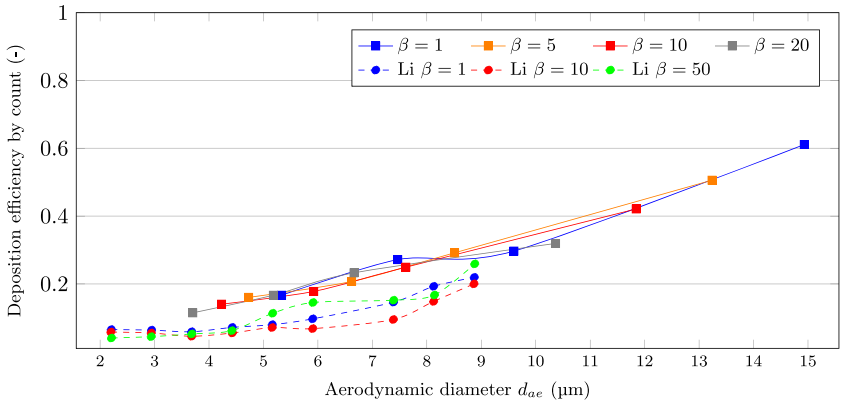

Fig. 19. Comparison of deposition efficiency of the tracheobronchial tree in dependence on the d_{ae} with Li et al. [32].

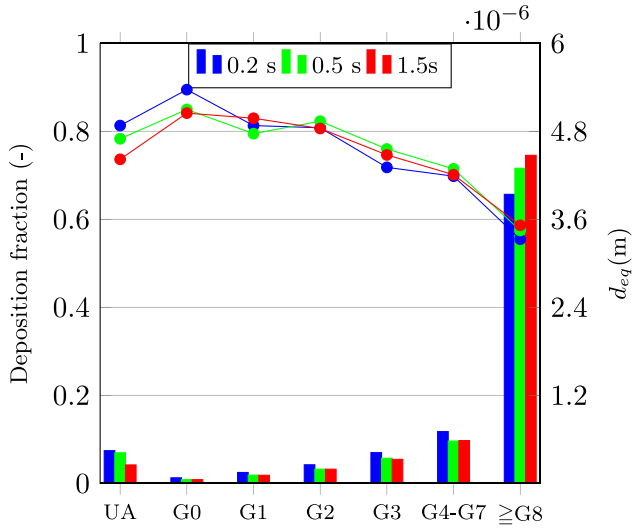

Fig. 20. Deposition fraction and mean equivalent diameter (d_{eq}) for each airway generation, categorized by particle release time during the inspiration cycle. The release times are divided into three periods: 0–0.2 s, 0.2–0.5 s, and 0.5–1.5 s.

a higher deposition fraction. In addition, the mean d_{eq} in this segment decreased with increasing release time and lower flow rate.

When considering deeper generations of branching, the discrepancies in d_{eq} gradually decrease. This can be attributed to the time required for the particles to travel from the release point to the considered segment. Moreover, the particles move at different velocities depending on their distance from the airway wall (especially in laminar flow regions), which further reduces the effect of the release time on the deposition fraction.

A slightly higher deposition fraction was observed for particles released during the first period (0–0.2 s), which was likely due to the higher flow rate in the initial part of the inspiratory cycle. However, the flow rate decreases after 0.5 s, resulting in a lower deposition rate for particles released later in the cycle. The probability of a particle reaching generations G8 and higher increases when it is released later in the cycle. A similar trend was observed for the mean d_{eq}, with the largest differences occurring in the upper airways and trachea (G0). The overall trend in d_{eq} as a function of release time is similar to the trend observed for the total deposition, as shown in Fig. 14.

Fig. 21 shows the cumulative deposition of the particles in each generation over time. A clear correlation with the flow rate was observed; the highest increase in deposition occurred during the period of the highest flow rate in the inspiration cycle. The time delay between deposition in the upper airways and tracheobronchial tree is attributed to the time required for particles to travel to the lower airways. The differences in deposition between individual generations are relatively small, which is consistent with the small dimensions of the fibers and high flow velocities. A slightly lower deposition was observed in the trachea (G0), likely due to its straight geometry and the reduced effect of inertial impaction compared to the curved trajectories in the bifurcations. As expected, the number of particles deposited during the hold-up time between inspiration cycles was negligible.

In medical applications, the fraction of particles deposited at the end of the first inspiration cycle is crucial because of the subsequent expiration phase. In our simulations, this value was approximately 70% in the bifurcation segments and 90% in the upper airways. The remaining particles are deposited at the beginning of the second inspiration cycle. However, in the real world, these particles can be exhaled during expiration, which was not considered in the current simulations. Kiasadegh et al. [33] presented a similar time-dependent deposition analysis for a geometry consisting of the upper airways and trachea. Their results, like ours, showed the highest deposition fraction at the beginning of the inspiration cycle. The observed discrepancies between our results and those of Kiasadegh et al. could be attributed to the differences in the inspiration profiles and airway geometries used. As described earlier, two types of deposition computations were employed in the simulations: a simple scheme (referred to as Case 2 in Section 2.2.2) and an orientation-dependent scheme (Case 3). The orientation-dependent scheme accounts for the orientation of the fiber relative to the airway wall, whereas the simple scheme does not. Notably, 93% of the particles were deposited via an orientation-dependent mechanism, with only 7% deposited via a simple scheme. This highlights the importance of using more complex orientation-dependent computations, especially for applications such as the delivery of pharmaceutical aerosols shaped as fibers or microrods, where the accurate prediction of deposition patterns is crucial. Using a simplified deposition scheme could lead to underestimation of the deposition fraction. However, it is important to acknowledge that the deposition mechanism can be influenced by the numerical time step. Moreover, the actual deposition process in an experimental setting is likely to be more complex than the simplified boundary conditions typically used in numerical studies.

4. Limitations of the study

This study involved several simplifying assumptions and limitations, which could be addressed in future research.

- The female airway model was generated via uniform linear scaling (factor 0.88) of a specific male model, based on average key dimensions (primarily tracheal) reported in the literature [43–45]. This simplification may not capture all region-specific or

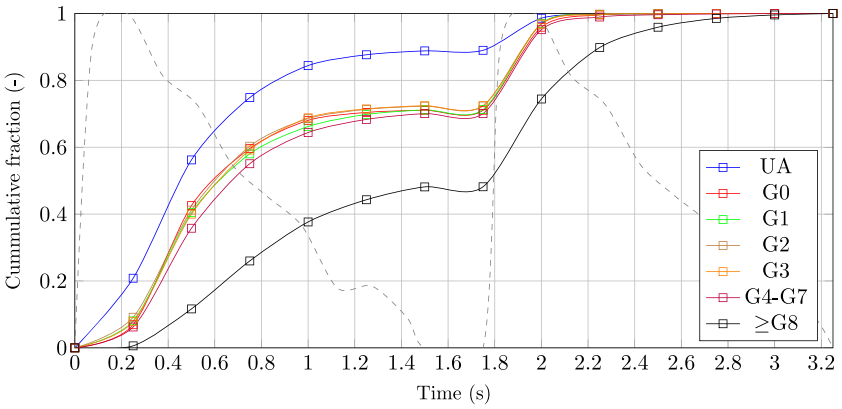

Fig. 21. Cumulative deposition fraction of deposited particles in each airway generation over time. The gray dashed line represents the normalized total flow rate during the inspiration cycle.

subtle non-linear morphological differences between male and female airways beyond overall size, nor does it account for inter-individual variability within the female population.

- The numerical simulations employed a simplified 'perfect sink' deposition mechanism, assuming that every contact between a fiber and the airway wall resulted in deposition. This assumption may not fully capture the complexities of particle–wall interactions even with the silicone oil coating used in the experimental airway replica to enhance capture [16,17], potentially leading to an overestimation of the deposition fraction compared to these specific in vitro results. However, this idealized capture simplification is often considered more representative of deposition on the highly efficient mucus-coated surfaces in actual human airways, where the presence of mucus on airway walls significantly increases the likelihood of particle capture upon contact.
- Only oral breathing was considered in this study, and the effect of the nasal cavity on airflow and particle deposition was neglected.
- The fibers were modeled as prolate spheroids, which may not perfectly represent their actual shape, which is often closer to cylindrical. More realistic particle shapes, such as superellipsoids or those with complex mass distributions, as presented by Wedel et al. [75,79], can be used in future simulations.
- The creeping flow particle-fluid interaction formulations were used in this study which may lead to discrepancies, mainly in the bifurcations. Non-creeping formulations [36,37] will be implemented as future work.
- The simulation was considered as isothermal, heat and mass transfer between the airflow, the nasal passage and mucus was neglected. The thermal plume, facial effects and surroundings of the human body, and air humidity were not considered either.
- The initial position and orientation of the particles released in the simulations were randomly generated, as it is challenging to measure these parameters experimentally. This uncertainty in the initial conditions could have affected the deposition patterns and introduced inaccuracies in the results.
- The subgrid-scale turbulence fluctuations smaller than the grid size were not considered in this study and can lead to small discrepancies in trajectories and orientations, and can influence exact deposition positions for particles near the walls, predominantly when reaching the peak flow rate. Modeling of the turbulence fluctuations, using, e.g., a Gaussian random filter [56], will be involved in future work investigating higher flow rates.
- A dilute air and one-way coupling model was used, assuming that the particles do not influence the airflow. This assumption may not be valid in all regions of the airway, particularly in the turbulent flow regime near bifurcations, where two-way coupling might be necessary for higher accuracy.
- Particle concentration was assumed to be low, and inter-particle collisions were neglected. Additionally, potential changes in the particle shape owing to collisions were not considered.
- Due to the time-consuming nature of the experiments, only one repetition was performed. Additional experimental data would be useful for a better estimation of the uncertainties.
- The effect of expiration on particle deposition was not considered in this study. This could be particularly relevant for particles deposited towards the end of the inspiration cycle, as they might be exhaled before having a chance to deposit permanently.
- Only one flow rate was simulated in this study. Systematic exploration of the influence of various breathing patterns was performed by e.g. [80,81], and hence similar trends in the deposition characteristics can be expected.

5. Conclusion

This study successfully applied the LBM in conjunction with the ELER method to simulate fiber transport and deposition in a realistic female airway model. A unique comparison of the deposition characteristics between numerical simulations and experiments conducted on the same airway geometry, extending to the 7th generation of branching, is presented. The results showed good agreement in the upper airways and trachea, but some discrepancies were observed in the bronchial bifurcations, likely owing to the challenges in capturing complex flow phenomena (such as Dean vortices and turbulence) using the ELER method.

In addition to comparing the ELER method with experimental data, its accuracy was also assessed by comparing it with simplified fiber deposition models that neglect fiber rotation (T-C and H–L methods). The ELER outperformed these simplified models, demonstrating its superior ability to predict fiber deposition in a realistic airway geometry and emphasizing the importance of orientation-dependent calculation of fiber transport and deposition.

This study also enabled a detailed analysis of the deposition patterns for different fiber size groups. Notably, the ELER method exhibited better agreement with the experimental data for smaller particles, indicating a higher accuracy in predicting the deposition fractions for these size ranges. Furthermore, the results confirmed that fibers with higher aspect ratios had a greater tendency to penetrate deeper into the lungs, which is consistent with previous findings.

A comparison of the deposition efficiency with literature data, using Stk as a basis for comparison, showed good agreement in the trachea. However, discrepancies were observed in the bifurcations, potentially owing to the differences in airway geometries and flow regimes between the studies. The use of a realistic, transient inspiration profile in our simulations led to a higher deposition efficiency compared to studies that employed steady flow conditions, likely owing to the higher peak velocities and resulting higher Stk in our simulations.

The numerical analysis revealed that particles released at the beginning of the inspiration cycle, when the flow rates were the highest, were more likely to deposit in the upper airways. This finding highlights the importance of considering initial high flow rates when designing drug delivery strategies. For instance, adjusting the release timing to avoid this initial phase could help prevent unwanted deposition in the upper airways. No significant differences in deposition were observed for particles released after the first third of the inspiration cycle, suggesting that the initial high flow rates had the greatest impact on the deposition location. Furthermore, only negligible differences in deposition were found among the various branching segments, indicating a relatively uniform distribution of deposition throughout the tracheobronchial tree. Approximately 70% of the particles were deposited during the first inspiration cycle.

Notably, the orientation-dependent deposition mechanism, which accounts for the angle of the fiber relative to the airway wall, was activated in 93% of the particles. This emphasizes its crucial role in accurately predicting deposition, particularly for applications such as locally targeted drug delivery, in which precise control over the deposition location is essential.

Simulating fibrous particles in realistic airway geometries using a realistic breathing profile provides valuable insights into optimizing the inhalation process and predicting fiber deposition patterns. However, the results also demonstrated that current numerical techniques for fiber modeling, specifically ELER, and the drag models H–L and T-C, still exhibit some discrepancies compared to the experimental data, especially in the branching regions. Further research is needed to improve these techniques and expand their applicability, ultimately enabling them to replace or complement experimental studies in a wider range of scenarios and contributing to the ongoing development of effective medical treatments.

This study also highlights a key difference between spherical and fibrous particles: fibers exhibit a greater ability to bypass the upper airways and penetrate deeper into the lungs. This finding has important implications for understanding the potential health risks associated with inhalation of different types of particles and for developing targeted drug delivery strategies that can effectively reach specific regions of the respiratory system.

Finally, it is crucial to consider the influence of individual airway geometries and breathing patterns on particle deposition. This study focused on a female airway model, but future research should investigate the differences in deposition between male, female, and child airways and evaluate the impact of various inhalation regimes. This knowledge is essential for developing personalized inhalation therapies tailored to the specific characteristics of individual patients.

CRediT authorship contribution statement

František Prinz: Writing – review & editing, Writing – original draft, Visualization, Validation, Software, Methodology, Investigation, Formal analysis, Data curation, Conceptualization. **Jana Kánská:** Writing – original draft, Visualization, Validation, Investigation, Data curation. **Jakub Elcner:** Supervision, Software, Data curation. **Ondřej Hájek:** Writing – review & editing, Data curation. **Adrian Kummerländer:** Writing – review & editing, Software. **Mathias J. Krause:** Writing – review & editing, Supervision. **Miroslav Jícha:** Supervision, Funding acquisition. **František Lízal:** Writing – review & editing, Supervision, Resources, Project administration, Methodology, Funding acquisition, Formal analysis, Conceptualization.

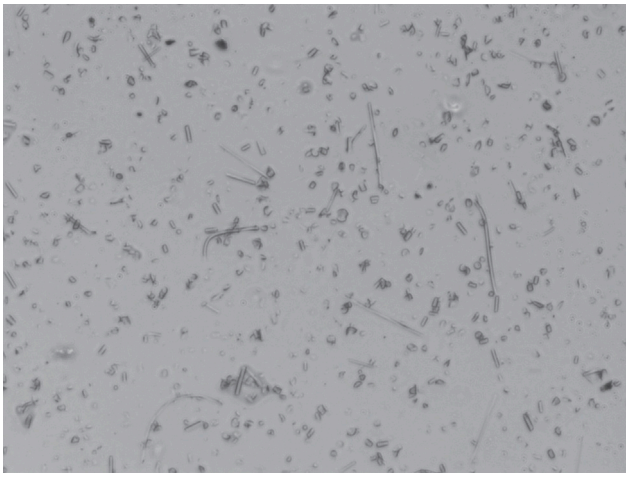

Fig. A.22. A representative micrograph showing collected glass fibers on a filter membrane.

Ethics statement

The author's declare that all procedures were performed in compliance with relevant laws and institutional guidelines.

Declaration of Generative AI and AI-assisted technologies in the writing process

During the preparation of this study, the authors used ChatGPT, Grammarly, and PaperPal to improve the language and readability. After using these tools, the authors reviewed and edited the content as needed and took full responsibility for the contents of the published article.

Declaration of competing interest

All authors declare that they have no conflicts of interest.

Acknowledgments

This work was supported by the Ministry of Education, Youth and Sports of the Czech Republic through the e-INFRA CZ (ID: 90254), by the Czech Science Foundation grant 22-20357S, and by the internal research project of Brno University of Technology, Czechia, reg. no. FSI-S-23-8192. The authors express gratitude to Pavel Fröml for conducting a series of experimental measurements.

Appendix. Detail to the experimental setup

See Fig. A.22 and Table A.2.

Data availability

The data used in this article are accessible in the Zenodo repository under the following DOI: 10.5281/zenodo.15166271.

Table A.2
Summary statistics of the total fiber counts and their length $2a$ and thickness d_p obtained by the experimental measurement.

Segment no.	No. of particles	Mean of d_p (μm)	Std. deviation of d_p (μm)	Mean of $2a$ (μm)	Std. deviation of $2a$ (μm)
1	325 264	2.0	1.3	15.8	14.5
2	96 341	2.4	1.2	18.2	15.3
3	37 160	1.9	1.0	20.1	15.9
4	42 206	1.7	0.9	14.7	8.3
5	43 583	1.9	1.1	14.8	11.5
6	42 106	2.2	1.8	17.0	14.0
7	36 242	1.6	0.6	13.7	9.4
8	29 820	2.4	1.8	13.9	9.6
9	26 608	1.4	0.6	14.3	8.3
10	20 644	1.7	0.9	13.7	11.6
11	18 351	1.6	0.7	21.3	18.5
12	22 021	2.2	1.9	21.7	15.9
13	83 954	1.9	0.7	14.3	10.3
14	30 278	1.4	0.6	21.8	28.9
15	22 021	1.9	1.1	15.7	12.8
16	112 397	1.8	0.6	15.9	11.7
17	26 608	1.9	0.8	21.2	13.7
18	53 676	1.8	0.9	19.2	24.6
19	61 016	1.9	0.7	21.4	24.4
20	23 397	1.3	0.5	13.6	7.6
21	37 160	1.5	0.8	15.1	10.6
22	38 995	1.7	0.5	13.8	9.6
13o	856 273	1.5	0.6	17.4	15.9
14o	585 743	1.5	0.7	16.2	13.9
15o	757 403	1.6	0.7	16.7	14.8
16o	1 031 666	1.6	0.7	17.3	15.2
17o	340 679	1.5	0.6	16.5	16.9
18o	1 087 424	1.6	0.8	17.4	16.3
19o	837 929	1.6	0.7	16.3	14.3
20o	347 844	1.5	0.7	16.8	15.0
21o	847 405	1.7	0.7	16.8	15.6
22o	1 047 117	1.6	0.7	16.1	14.9

References

[1] O.P. Soldin, D.R. Mattison, Sex differences in pharmacokinetics and pharmacodynamics, Clin. Pharmacokinet. 48 (3) (2009) 143–157, http://dx.doi.org/10.2165/00003088-200948030-00001.

[2] C.M. Madla, F.K. Gavins, H.A. Merchant, M. Orlu, S. Murdan, A.W. Basit, Let's talk about sex: Differences in drug therapy in males and females, Adv. Drug Deliv. Rev. 175 (2021) 113804, http://dx.doi.org/10.1016/j.addr.2021.05.014.

[3] S. Sharifi, G. Caracciolo, D. Pozzi, L. Digiacomo, J. Swann, H.E. Daldrup-Link, M. Mahmoudi, The role of sex as a biological variable in the efficacy and toxicity of therapeutic nanomedicine, Adv. Drug Deliv. Rev. 174 (2021) 337–347, http://dx.doi.org/10.1016/j.addr.2021.04.028.

[4] S. Cheng, J. Butler, S. Gandevia, L. Bilston, Movement of the tongue during normal breathing in awake healthy humans, J. Physiol. 586 (17) (2008) 4283–4294, http://dx.doi.org/10.1113/jphysiol.2008.156430.

[5] A. LoMauro, A. Aliverti, Sex differences in respiratory function, Breathe 14 (2) (2018) 131–140, http://dx.doi.org/10.1183/20734735.000318.

[6] M.A. Carey, J.W. Card, J.W. Voltz, D.R. Germolec, K.S. Korach, D.C. Zeldin, The impact of sex and sex hormones on lung physiology and disease: lessons from animal studies, Am. J. Physiol.-Lung Cell. Mol. Physiol. 293 (2) (2007) L272–L278, http://dx.doi.org/10.1152/ajplung.00174.2007.

[7] T. Mekonnen, X. Cai, C. Burchell, H. Gholizadeh, S. Cheng, A review of upper airway physiology relevant to the delivery and deposition of inhalation aerosols, Adv. Drug Deliv. Rev. 191 (2022) 114530, http://dx.doi.org/10.1016/j.addr.2022.114530.

[8] L. Shachar-Berman, S. Bhardwaj, Y. Ostrovski, P. Das, P. Koullapis, S. Kassinos, J. Sznitman, In silico optimization of fiber-shaped aerosols in inhalation therapy for augmented targeting and deposition across the respiratory tract, Pharmaceutics 12 (3) (2020) 230, http://dx.doi.org/10.3390/pharmaceutics12030230.

[9] J. Marijnlssen, A. Zeckendorf, S. Lemkowltz, H. Bibo, Transport and deposition of uniform respirable fibres in a physical lung model, J. Aerosol Sci. 22 (1991) S859–S862, http://dx.doi.org/10.1016/S0021-8502(05)80234-4.

[10] T. Myojo, M. Takaya, Estimation of fibrous aerosol deposition in upper bronchi based on experimental data with model bifurcation, Ind. Health 39 (2) (2001) 141–149, http://dx.doi.org/10.2486/indhealth.39.141.

[11] E.R. Weibel, A.F. Cournand, D.W. Richards, Morphometry of the Human Lung, vol. 1, Springer, 1963, http://dx.doi.org/10.1007/978-3-642-87553-3.

[12] W.-C. Su, Y.S. Cheng, Deposition of fiber in a human airway replica, J. Aerosol Sci. 37 (11) (2006) 1429–1441, http://dx.doi.org/10.1016/j.jaerosci.2006.01.015.

[13] Y. Feng, C. Kleinstreuer, Analysis of non-spherical particle transport in complex internal shear flows, Phys. Fluids 25 (2013) 1904, http://dx.doi.org/10.1063/1.4821812.

[14] W.-C. Su, Y.S. Cheng, Fiber deposition pattern in two human respiratory tract replicas, Inhal. Toxicol. 18 (10) (2006) 749–760, http://dx.doi.org/10.1080/08958370600748513.

[15] Y. Zhou, W.-C. Su, Y.S. Cheng, Fiber deposition in the tracheobronchial region: Experimental measurements, Inhal. Toxicol. 19 (13) (2007) 1071–1078, http://dx.doi.org/10.1080/08958370701626634.

[16] W.-C. Su, Y.S. Cheng, Deposition of man-made fibers in human respiratory airway casts, J. Aerosol Sci. 40 (3) (2009) 270–284, http://dx.doi.org/10.1016/j.jaerosci.2008.11.003.

[17] M. Belka, F. Lizal, J. Jedelsky, J. Elcner, P.K. Hopke, M. Jicha, Deposition of glass fibers in a physically realistic replica of the human respiratory tract, J. Aerosol Sci. 117 (2018) 149–163, http://dx.doi.org/10.1016/j.jaerosci.2017.11.006.

[18] F. Lizal, M. Cabalka, M. Maly, J. Elcner, M. Belka, E. Lizalova Sujanska, A. Farkas, P. Starha, O. Pech, O. Misik, J. Jedelsky, M. Jicha, On the behavior of inhaled fibers in a replica of the first airway bifurcation under steady flow conditions, Aerosol Sci. Technol. 56 (4) (2022) 367–381, http://dx.doi.org/10.1080/02786826.2022.2027334.

[19] C. Kleinstreuer, Y. Feng, Computational analysis of non-spherical particle transport and deposition in shear flow with application to lung aerosol dynamics—A review, J. Biomech. Eng. 135 (021008) (2013) http://dx.doi.org/10.1115/1.4023236.

[20] I.A. Lasso, P. Weidman, Stokes drag on hollow cylinders and conglomerates, Phys. Fluids 29 (12) (1986) 3921–3934, http://dx.doi.org/10.1063/1.865732.

[21] A. Haider, O. Levenspiel, Drag coefficient and terminal velocity of spherical and nonspherical particles, Powder Technol. 58 (1) (1989) 63–70, http://dx.doi.org/10.1016/0032-5910(89)80008-7.

[22] S. Tran-Cong, M. Gay, E.E. Michaelides, Drag coefficients of irregularly shaped particles, Powder Technol. 139 (1) (2004) 21–32, http://dx.doi.org/10.1016/j.powtec.2003.10.002.

[23] W. Stöber, Dynamic shape factors of nonspherical aerosol particles, Assess. Airborne Part. (1972) 249–289.

[24] K. Inthavong, J. Wen, Z. Tian, J. Tu, Numerical study of fibre deposition in a human nasal cavity, J. Aerosol Sci. 39 (2008) 253–265, http://dx.doi.org/10.1016/j.jaerosci.2007.11.007.

[25] A. Farkas, F. Lizal, J. Elcner, J. Jedelsky, M. Jicha, Numerical simulation of fibre deposition in oral and large bronchial airways in comparison with experiments, J. Aerosol Sci. 136 (2019) 1–14, http://dx.doi.org/10.1016/j.jaerosci.2019.06.003.

[26] X. Chen, W. Zhong, J. Tom, C. Kleinstreuer, Y. Feng, X. He, Experimental-computational study of fibrous particle transport and deposition in a bifurcating lung model, Particuology 28 (2016) 102–113, http://dx.doi.org/10.1016/j.partic.2016.02.002.

[27] L. Tian, G. Ahmadi, Z. Wang, P.K. Hopke, Transport and deposition of ellipsoidal fibers in low Reynolds number flows, J. Aerosol Sci. 45 (2012) 1–18, http://dx.doi.org/10.1016/j.jaerosci.2011.09.001.

[28] L. Tian, G. Ahmadi, Fiber transport and deposition in human upper tracheobronchial airways, J. Aerosol Sci. (60) (2013) 1–20, http://dx.doi.org/10.1016/j.jaerosci.2013.02.001.

[29] K.T. Shanley, G. Ahmadi, P.K. Hopke, Y.-S. Cheng, Simulated airflow and rigid fiber behavior in a realistic nasal airway model, Part. Sci. Technol. 36 (2) (2018) 131–140, http://dx.doi.org/10.1080/02726351.2016.1208694.

[30] J. Li, J. Ma, J. Dong, W. Yang, G. Ahmadi, J. Tu, L. Tian, Microfiber transport characterization in human nasal cavity – Effect of fiber length, J. Aerosol Sci. 160 (2022) 105908, http://dx.doi.org/10.1016/j.jaerosci.2021.105908.

[31] J. Li, J. Ma, G. Ahmadi, J. Dong, W. Yang, J. Tu, L. Tian, Shear induced lift and rotation on MicroFiber deposition in low Reynolds number flows, J. Aerosol Sci. 167 (2023) 106094, http://dx.doi.org/10.1016/j.jaerosci.2022.106094.

[32] J. Li, J. Ma, J. Dong, W. Yang, J. Tu, L. Tian, Total and regional microfiber transport characterization in a 15th - Generation human respiratory airway, Comput. Biol. Med. 163 (2023) 107180, http://dx.doi.org/10.1016/j.compbiomed.2023.107180.

[33] M. Kiasadegh, H. Emdad, G. Ahmadi, O. Abouali, Transient numerical simulation of airflow and fibrous particles in a human upper airway model, J. Aerosol Sci. 140 (2020) 105480, http://dx.doi.org/10.1016/j.jaerosci.2019.105480.

[34] M.M. Tavakol, E. Ghahramani, O. Abouali, M. Yaghoubi, G. Ahmadi, Deposition fraction of ellipsoidal fibers in a model of human nasal cavity for laminar and turbulent flows, J. Aerosol Sci. 113 (2017) 52–70, http://dx.doi.org/10.1016/j.jaerosci.2017.07.008.

[35] M. Abolhassantash, M.M. Tavakol, O. Abouali, M. Yaghoubi, G. Ahmadi, Deposition fraction of ellipsoidal fibers in the human nasal cavity- Influence of non-creeping formulation of hydrodynamic forces and torques, Int. J. Multiph. Flow 126 (2020) 103238, http://dx.doi.org/10.1016/j.ijmultiphaseflow.2020.103238.

[36] M. Zastawny, G. Mallouppas, F. Zhao, B. van Wachem, Derivation of drag and lift force and torque coefficients for non-spherical particles in flows, Int. J. Multiph. Flow 39 (2012) 227–239, http://dx.doi.org/10.1016/j.ijmultiphaseflow.2011.09.004.

[37] R. Ouchene, M. Khalij, B. Arcen, A. Tanière, A new set of correlations of drag, lift and torque coefficients for non-spherical particles and large Reynolds numbers, Powder Technol. 303 (2016) 33–43, http://dx.doi.org/10.1016/j.powtec.2016.07.067.

[38] A.A. Mofakham, G. Ahmadi, On random walk models for simulation of particle-laden turbulent flows, Int. J. Multiph. Flow 122 (2020) 103157, http://dx.doi.org/10.1016/j.ijmultiphaseflow.2019.103157.

[39] L. Tian, G. Ahmadi, Computational modeling of fiber transport in human respiratory airways—A review, Exp. Comput. Multiph. Flow 3 (1) (2021) 1–20, http://dx.doi.org/10.1007/s42757-020-0061-7.

[40] T. Henn, G. Thäter, W. Dörfler, H. Nirschl, M. Krause, Parallel dilute particulate flow simulations in the human nasal cavity, Comput. & Fluids 124 (2016) 197–207, http://dx.doi.org/10.1016/j.compfluid.2015.08.002.

[41] F. Prinz, J. Pokorný, J. Elcner, F. Lízal, O. Mišík, M. Malý, M. Bělka, N. Hafen, A. Kummerländer, M.J. Krause, J. Jedelský, M. Jícha, Comprehensive experimental and numerical validation of Lattice Boltzmann fluid flow and particle simulations in a child respiratory tract, Comput. Biol. Med. 170 (2024) 107994, http://dx.doi.org/10.1016/j.compbiomed.2024.107994.

[42] F. Lizal, J. Elcner, P.K. Hopke, J. Jedelsky, M. Jicha, Development of a realistic human airway model, Proc. Inst. Mech. Eng. Part H J. Eng. Med. 226 (3) (2012) 197–207, http://dx.doi.org/10.1177/0954411911430188.

[43] N. Griscom, M. Wohl, Dimensions of the growing trachea related to age and gender, Am. J. Roentgenol. 146 (2) (1986) 233–237, http://dx.doi.org/10.2214/ajr.146.2.233, PMID: 3484568.

[44] T.R. Martin, R.G. Castile, J.J. Fredberg, M.E. Wohl, J. Mead, Airway size is related to sex but not lung size in normal adults, J. Appl. Physiol. 63 (5) (1987) 2042–2047, http://dx.doi.org/10.1152/jappl.1987.63.5.2042, Publisher: American Physiological Society.

[45] A.W. Sheel, J.A. Guenette, R. Yuan, L. Holy, J.R. Mayo, A.M. McWilliams, S. Lam, H.O. Coxson, Evidence for dysanapsis using computed tomographic imaging of the airways in older ex-smokers, J. Appl. Physiol. 107 (5) (2009) 1622–1628, http://dx.doi.org/10.1152/japplphysiol.00562.2009, Publisher: American Physiological Society.

[46] ICRP, Human respiratory tract model for radiological protection, Ann. ICRP 66 (1994) 1–3.

[47] N. Jahani, S. Choi, J. Choi, K. Iyer, E.A. Hoffman, C.-L. Lin, Assessment of regional ventilation and deformation using 4D-CT imaging for healthy human lungs during tidal breathing, J. Appl. Physiol. 119 (10) (2015) 1064–1074, http://dx.doi.org/10.1152/japplphysiol.00339.2015.

[48] W.H. Organization, et al., Determination of Airborne Fibre Number Concentrations: A Recommended Method, by Phase-Contrast Optical Microscopy (Membrane Filter Method), World Health Organization, 1997, p. 53.

[49] T. Krüger, H. Kusumaatmaja, A. Kuzmin, O. Shardt, G. Silva, E.M. Viggen, The Lattice Boltzmann Method: Principles and Practice, Graduate Texts in Physics, Springer International Publishing, 2017, http://dx.doi.org/10.1007/978-3-319-44649-3.

[50] A. Kummerländer, F. Bukreev, S.F.R. Berg, M. Dorn, M.J. Krause, Advances in computational process engineering using lattice Boltzmann methods on high performance computers, in: W.E. Nagel, D.H. Kröner, M.M. Resch (Eds.), High Performance Computing in Science and Engineering '22, Springer Nature Switzerland, 2024, pp. 233–247, http://dx.doi.org/10.1007/978-3-031-46870-4_16.

[51] M. Haussmann, F. Ries, J.B. Jeppener-Haltenhoff, Y. Li, M. Schmidt, C. Welch, L. Illmann, B. Böhm, H. Nirschl, M.J. Krause, A. Sadiki, Evaluation of a near-wall-modeled large eddy lattice Boltzmann method for the analysis of complex flows relevant to IC engines, Computation 8 (2) (2020-05-05) 43, http://dx.doi.org/10.3390/computation8020043.

[52] S. Chapman, T.G. Cowling, The Mathematical Theory of Non-Uniform Gases: An Account of the Kinetic Theory of Viscosity, Thermal Conduction and Diffusion in Gases, Cambridge University Press, 1990.

[53] S. Hou, J.D. Sterling, S. Chen, G.D. Doolen, A lattice Boltzmann subgrid model for high Reynolds number flows, 1994, arXiv: Cellular Automata and Lattice Gases.

[54] I.B. Celik, Z.N. Cehreli, I. Yavuz, Index of resolution quality for large eddy simulations, J. Fluids Eng. 127 (5) (2005) 949–958, http://dx.doi.org/10.1115/1.1990201.

[55] M. Sommerfeld, O.L. Sgrott, M.A. Taborda, P. Koullapis, K. Bauer, S. Kassinos, Analysis of flow field and turbulence predictions in a lung model applying RANS and implications for particle deposition, Eur. J. Pharm. Sci. 166 (2021) 105959, http://dx.doi.org/10.1016/j.ejps.2021.105959.

[56] M. Salmanzadeh, M. Rahnama, G. Ahmadi, Effect of sub-grid scales on large eddy simulation of particle deposition in a turbulent channel flow, Aerosol Sci. Technol. 44 (9) (2010) 796–806, http://dx.doi.org/10.1080/02786826.2010.492052.

[57] H. Sajjadi, M. Salmanzadeh, G. Ahmadi, S. Jafari, Simulations of indoor airflow and particle dispersion and deposition by the lattice Boltzmann method using LES and RANS approaches, Build. Environ. 102 (2016) 1–12, http://dx.doi.org/10.1016/j.buildenv.2016.03.006.

[58] E. Ghahramani, O. Abouali, H. Emdad, G. Ahmadi, Numerical investigation of turbulent airflow and microparticle deposition in a realistic model of human upper airway using LES, Comput. & Fluids 157 (2017) 43–54, http://dx.doi.org/10.1016/j.compfluid.2017.08.003.

[59] P. Koullapis, S.C. Kassinos, J. Muela, C. Perez-Segarra, J. Rigola, O. Lehmkuhl, Y. Cui, M. Sommerfeld, J. Elcner, M. Jicha, I. Saveljic, N. Filipovic, F. Lizal, L. Nicolaou, Regional aerosol deposition in the human airways: The SimInhale benchmark case and a critical assessment of in silico methods, Eur. J. Pharm. Sci. 113 (2018) 77–94, http://dx.doi.org/10.1016/j.ejps.2017.09.003.

[60] P. Skordos, Initial and boundary conditions for the lattice Boltzmann method, Phys. Rev. E 48 (1993) 4823–4842, http://dx.doi.org/10.1103/PhysRevE.48.4823.

[61] M. Bouzidi, M. Firdaouss, P. Lallemand, Momentum transfer of a Boltzmann-lattice fluid with boundaries, Phys. Fluids 13 (2001) 3452–3459, http://dx.doi.org/10.1063/1.1399290.

[62] A. Lintermann, W. Schröder, Simulation of aerosol particle deposition in the upper human tracheobronchial tract, Eur. J. Mech. B Fluids 63 (2017) 73–89, http://dx.doi.org/10.1016/j.euromechflu.2017.01.008.

[63] F.-G. Fan, G. Ahmadi, A sublayer model for wall deposition of ellipsoidal particles in turbulent streams, J. Aerosol Sci. 26 (5) (1995) 813–840, http://dx.doi.org/10.1016/0021-8502(95)00021-4.

[64] H. Brenner, The Stokes resistance of an arbitrary particle—IV arbitrary fields of flow, Chem. Eng. Sci. 19 (10) (1964) 703–727, http://dx.doi.org/10.1016/0009-2509(64)85084-3.

[65] E.Y. Harper, I.-D. Chang, Maximum dissipation resulting from lift in a slow viscous shear flow, J. Fluid Mech. 33 (2) (1968) 209–225, http://dx.doi.org/10.1017/S0022112068001254.

[66] Y. Cui, J. Ravnik, M. Hriberšek, P. Steinmann, On constitutive models for the momentum transfer to particles in fluid-dominated two-phase flows, in: H. Altenbach, F. Jablonski, W.H. Müller, K. Naumenko, P. Schneider (Eds.), Advances in Mechanics of Materials and Structural Analysis: in Honor of Reinhold Kienzler, in: Advanced Structured Materials, Springer International Publishing, Cham, 2018, pp. 1–25, http://dx.doi.org/10.1007/978-3-319-70563-7_1.

[67] Y. Cui, J. Ravnik, M. Hriberšek, P. Steinmann, Towards a unified shear-induced lift model for prolate spheroidal particles moving in arbitrary non-uniform flow, Comput. & Fluids 196 (2020) 104323, http://dx.doi.org/10.1016/j.compfluid.2019.104323.

[68] G.B. Jeffery, The motion of ellipsoidal particles immersed in a viscous fluid, Proc. R. Soc. Lond. Ser. A Contain. Pap. A Math. Phys. Charact. 102 (715) (1922) 161–179.

[69] F.-G. Fan, G. Ahmadi, A sublayer model for wall deposition of ellipsoidal particles in turbulent streams, J. Aerosol Sci. 26 (5) (1995) 813–840, http://dx.doi.org/10.1016/0021-8502(95)00021-4.

[70] A. Kummerlander, T. Bingert, F. Bukreev, L.E. Czelusniak, D. Dapelo, N. Hafen, M. Heinzelmann, S. Ito, J. Jeßberger, H. Kusumaatmaja, J.E. Marquardt, M. Rennick, T. Pertzel, F. Prinz, M. Sadric, M. Schecher, S. Simonis, P. Sitter, D. Teutscher, M. Zhong, M.J. Krause, OpenLB release 1.7: Open source lattice Boltzmann code, 2024, http://dx.doi.org/10.5281/zenodo.10684609.

[71] A. Kummerlander, T. Bingert, F. Bukreev, L.E. Czelusniak, D. Dapelo, S. Englert, N. Hafen, M. Heinzelmann, S. Ito, J. JeÃŸberger, F. Kaiser, E. Kummer, H. Kusumaatmaja, J.E. Marquardt, M. Rennick, T. Pertzel, F. Prinz, M. Sadric, M. Schecher, S. Simonis, P. Sitter, D. Teutscher, M. Zhong, M.J. Krause, OpenLB user guide 1.7, 2024, http://dx.doi.org/10.5281/zenodo.13293033.

[72] M. Krause, A. Kummerländer, S. Avis, H. Kusumaatmaja, D. Dapelo, F. Klemens, M. Gaedtke, N. Hafen, A. Mink, R. Trunk, J. Marquardt, M. Maier, M. Haussmann, S. Simonis, OpenLB–open source lattice Boltzmann code, Comput. Math. Appl. 81 (2021) 258–288, http://dx.doi.org/10.1016/j.camwa.2020.04.033.

[73] K. Shanley, G. Ahmadi, A numerical model for simulating the motions of ellipsoidal fibers suspended in low Reynolds number shear flows, Aerosol Sci. Technol. 45 (2011) 838–848, http://dx.doi.org/10.1080/02786826.2011.566293.

[74] Y. Cui, J. Ravnik, M. Hriberšek, P. Steinmann, A novel model for the lift force acting on a prolate spheroidal particle in an arbitrary non-uniform flow. Part I. lift force due to the streamwise flow shear, Int. J. Multiph. Flow 104 (2018) 103–112, http://dx.doi.org/10.1016/j.ijmultiphaseflow.2018.03.007.

[75] J. Wedel, P. Steinmann, M. Štrakl, M. Hriberšek, J. Ravnik, Shape matters: Lagrangian tracking of complex nonspherical microparticles in superellipsoidal approximation, Int. J. Multiph. Flow 158 (2023) 104283, http://dx.doi.org/10.1016/j.ijmultiphaseflow.2022.104283.

[76] J. Elcner, F. Lizal, J. Jedelsky, M. Jicha, M. Chovancova, Numerical investigation of inspiratory airflow in a realistic model of the human tracheobronchial airways and a comparison with experimental results, Biomech. Model. Mechanobiol. 15 (2) (2016) 447–469, http://dx.doi.org/10.1007/s10237-015-0701-1.

[77] A. Naseri, S. Shaghaghian, O. Abouali, G. Ahmadi, Numerical investigation of transient transport and deposition of microparticles under unsteady inspiratory flow in human upper airways, Respir. Physiol. Neurobiol. 244 (2017) 56–72, http://dx.doi.org/10.1016/j.resp.2017.06.005.

[78] H. Bahmanzadeh, O. Abouali, G. Ahmadi, Unsteady particle tracking of microparticle deposition in the human nasal cavity under cyclic inspiratory flow, J. Aerosol Sci. 101 (2016) 86–103, http://dx.doi.org/10.1016/j.jaerosci.2016.07.010.

[79] J. Wedel, P. Steinmann, F. Prinz, F. Lízal, M. Hriberšek, J. Ravnik, Mass distribution impacts on particle translation and orientation dynamics in dilute flows, Powder Technol. 452 (2025) 120424, http://dx.doi.org/10.1016/j.powtec.2024.120424.

[80] K. Kuga, R. Kizuka, N.D. Khoa, K. Ito, Effect of transient breathing cycle on the deposition of micro and nanoparticles on respiratory walls, Comput. Methods Programs Biomed. 236 (2023) 107501, http://dx.doi.org/10.1016/j.cmpb.2023.107501.

[81] H. Liu, S. Ma, T. Hu, D. Ma, Computational investigation of flow characteristics and particle deposition patterns in a realistic human airway model under different breathing conditions, Respir. Physiol. Neurobiol. 314 (2023) 104085, http://dx.doi.org/10.1016/j.resp.2023.104085.